Università degli Studi di Milano Bicocca
Dipartimento di Scienze dei Materiali

Ph. D. in Materials Science - XXIV cycle

Dye Sensitized Solar Cells: materials and processes

Ph. D. Thesis of:
Dell'Orto Elisa Camilla
042053
Thesis presented for the degree of Doctor Europaeus

Supervisor: **Prof. Alessandro Abbotto**
Dean of the Doctorate: **Prof. Gianpaolo Brivio**

January 2012

Contents

Introduction

The conversion of solar energy to generate electricity is becoming very important in recent years, as global population growth and the limited amount of fossil fuels have increased the interest in alternative energy sources.

In solar cells devices it is possible to obtain electrical current through the charge separation that occurs by the absorption of electromagnetic radiation at the interface between two materials with different conduction proprieties.

The most common solar cell devices are solid-state cells, where the junction between a p-doped and a n-doped semiconductors creates a depletion zone in which there is the creation of excitons, and electrons are separated from the hole because of the change in the energy bands of two semiconductors, indeed caused by their junction.

However, there are several alternatives to these devices, an important position is occupied by Dye Sensitized Solar Cells (DSSCs) [**1, 2**]

which, although have not yet reached efficiency comparable with the solid-state cells (at the moment the record efficiency for a DSSC is 12.3% [**3**], that is about an half of a polycrystalline silicon cell), have a great interest due to their low cost, the availability of materials and ease of preparation [**4, 5, 6, 7**].

Though much progress was achieved in terms of intrinsic cell stability and up scaling, there are a lot of problems that need to be solved to allow industrialization and a large production of these devices. Main problems concerns low stability, low efficiency, low scalability. Low stability is mainly related to degradation in sealing material and to corrosive action of ionic liquid electrolyte. For this region in last years a lot a studies have concerned solid hole transporting materials to replace liquid electrolyte. To improve efficiency a lot of sensitizer were been studied, to improve the harvesting of light. Also the study of alternative photo-anode structures could be an interesting field in this direction. The up-scaling problems is connected to the use of some low available materials (such as platinum or ruthenium) and the presence of high sheet resistances.

The work made during these years had the presuppositions to analyze different aspects of DSSCs optimization, to understood the complexity of devices and the influence of different components in

overall results. For this reason different materials have been studied and different diagnostic technique have been investigated.

The study began in a laboratory where DSSCs fabrication was start-up process. For this reason a part of the work regarded the adjustment of a protocol to realize DSSC devices, by the choosing of materials and equipments, in collaboration with different institutes.

During the thesis the DSSCs optimization was analyzed mainly through two strategies: the study of new sensitizers and the study of alternatives materials for photo-cathode fabrication. Two class of sensitizers were be analyzed: squaraine dyes and cyclometalated-based dyes. Then a study on dye-loading process will be presented, with implication in an industrialization process.

For the photo-cathode fabrication two different materials were studied, a carbon based material and a polymeric material.

Then a part of the work concerned the study of devices analysis system. In particular electrochemical impedance spectroscopy was studied to propose a new set up to analyze electric processes in different cell components.

CHAPTER 1

Theoretical background and state of art

1.1. Photovoltaic energy conversion principles

1.1.1. Solar spectrum. Sun can be approximated to a black body at the temperature of 5800 K. So solar spectrum can be find using Planck's distribution:

$$I(\nu)d\nu = \frac{2h\nu^3}{c^2}\frac{1}{e^{\frac{h\nu}{kT}}-1}d\nu \tag{1.1.1}$$

where $I(\nu)$ is the power of electromagnetic radiation at frequency ν radiated per unit area of emitting surface in the normal direction per unit solid angle per unit frequency by a black body at temperature T, h is the Planck constant, c is the speed of light in the vacuum and k is the Boltzmann constant.[8]

As it passes through the atmosphere, solar radiation is attenuated by scattering and absorption; the more atmosphere through which it passes, the greater the attenuation is. Absorption concerns

UV region (it's due to oxygen, ozone, nitrous oxide and methane), IR region (water vapor) and infrared region (carbon dioxide). The effect of scattering is to remove high energy radiation in direct sunlight.

If L_0 is the thickness of an atmosphere layer, and L is the path length of the light through this layer, the air-mass (AM) coefficient is defined as:

$$AM = \frac{L}{L_0} \approx \frac{1}{cos\alpha} \tag{1.1.2}$$

where α is the zenith angle in degree.

AM0 corresponds to the extraterrestrial radiation, without atmospheric attenuation. For photovoltaic characterizations, the standard reference spectrum is AM1.5G, that corresponds to the total global irradiance at a zenith angle of 48.2° and good represents the overall yearly average for mid-latitudes. Figure 1.1.1 compares different spectra. The total irradiance is the integral of the curves on all wavelength radiation, for the reference spectrum $I_{AM1.5G} = 1000.4\,Wm^{-2}$.[**9**]

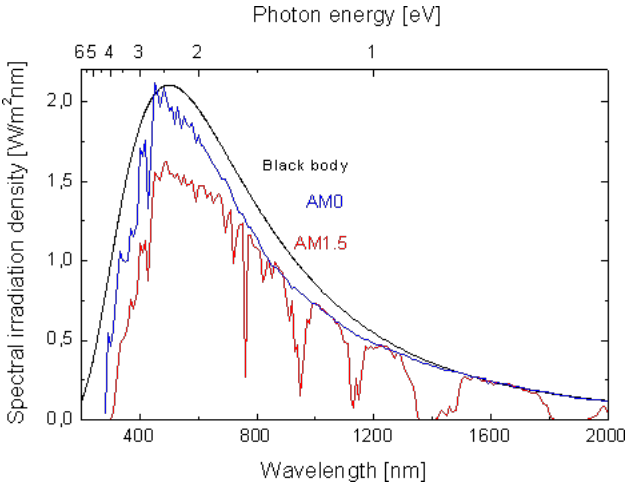

FIGURE 1.1.1. Spectra of a black body at T=5800 K, the extraterrestrial radiation (AM0) and the standard solar radiation (AM1.5G) [**10**].

1.1.2. Photovoltaic conversion. A photovoltaic device is, in general, a device with the ability to convert solar radiation into electrical power. This kind of device include p-n-junction solar cells, photo-electrochemical cells, DSSCs, photo-galvanic cells, and organic (plastic) solar cells. In general, the process of photovoltaic energy conversion can be divided into three steps:

(a) electronic excitation of the absorbing component of the converter by light absorption with concomitant electronic charge creation.

(b) Separation of the electronic charges.

(c) Charges collection.

The excitation can be an electron-hole pair in a semiconductor, an electronic excitation of a molecule, or the production of excitons.

The first to observe photovoltaic effect was Becquerel in 1839[**11**], by illuminating Pt electrodes coated with AgCl or AgBr into an acid solution. About 50 years later, Charles Fritts constructed the first true solar cells using junctions formed by coating the semiconductor selenium with an ultra thin, nearly transparent layer of gold.[**12**] The first silicon solar cells were made by Russel Ohl in 1941[**13**]. It was formed by cutting the ingot to include sections with both a p-type and n-type region and applying metal contacts.

Most photovoltaic devices to date have been formed by coupling a p-type semiconductor and a n-type one (p-n junction). Through the contact surface of two semiconductors, electrons flow from n-type material to p-type, while some holes move in the opposite direction (fig. 1.1.2). The n-type material thus acquires a slight positive charge, while the p-type becomes slightly negative. Around the junction area (depletion layer) a field is therefore generated, thought the p-type material to n-type. This layer prevents any further spread in the two verses of the charge carriers. [**14, 15**]

When a solar cell absorbs light radiation, if the photon energy $E = h\nu$ is less than the semiconductor energy gap E_g they do not can be captured by electrons since these would be brought to a energy level of the forbidden band gap level. If instead if $h\nu > E_g$ the electron captures a photon and is excited to the conduction band, leaving a hole in the valence band. When operating as a solar cell, the electrons excited to the conduction band flow from the p-type to the n-type side, while the holes left behind in the valence band flow in the opposite direction. If the two crystals are connected by a wire, the equilibrium is restored by a electrons flow from n to the crystal p. The absorption of radiation light causing a continuous electric current in the wire [**16**].

1.2. DSSCs principles

DSSCs exhibit a different mode of operation respect p-n junction cells [**17**]. Absorption occurs at a very specific location at the dye molecules attached to a porous semiconductor (usually TiO_2) medium (figure 1.2.1). In the dye-sensitized cell, photo-absorption excites an electron into a high energy level of a dye molecule adjacent to titania film. The excited electron quickly drops into the conduction band of the TiO_2 and is transported away from the generation

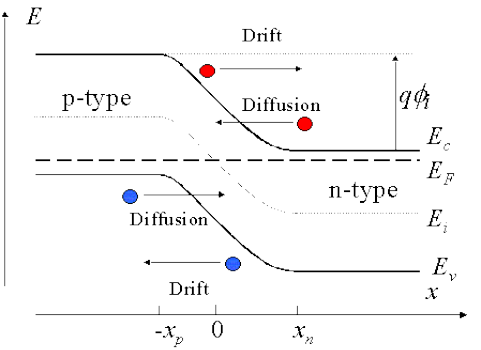

FIGURE 1.1.2. To reach thermal equilibrium, electrons/holes diffuse across the junction into the p-type/n-type region. This process leaves the ionized donors (acceptors) behind, creating a region around the junction, which is depleted of mobile carriers. This depletion region extends from$x = -x_p$ to $x = x_n$. The charge due to the ionized donors and acceptors causes an electric field, which in turn causes a drift of carriers in the opposite direction. The diffusion of carriers continues until the drift current balances the diffusion current, thereby reaching thermal equilibrium as indicated by a constant Fermi energy E_F.

site [**18, 19**]. The state from which electron was originally excited is replenished by electrons shuttled across a liquid medium. It is interesting to note how the light absorption and charge transport processes are largely decoupled.

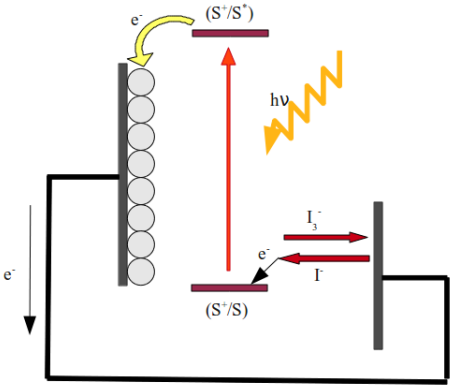

FIGURE 1.2.1. Scheme of function of a Dye Sensitized Solar Cell.

In fact in DSSCs there is an electron-conductive phase (n-type semiconductor) and a hole-conductive phase (redox species), that form an heterojunction. For this reason DSSC are majority carried device (efficiency is strongly depended on the ability to generate majority carriers), where electrons and holes are in two different chemical phases.[**20, 21, 22**]

1.2.1. DSSCs detailed electronic processes. DSSCs are photo-electrochemical devices where several electron transfer processes take place in the same time with different time scales (figure 1.2.2) [**23, 24, 25, 26**].

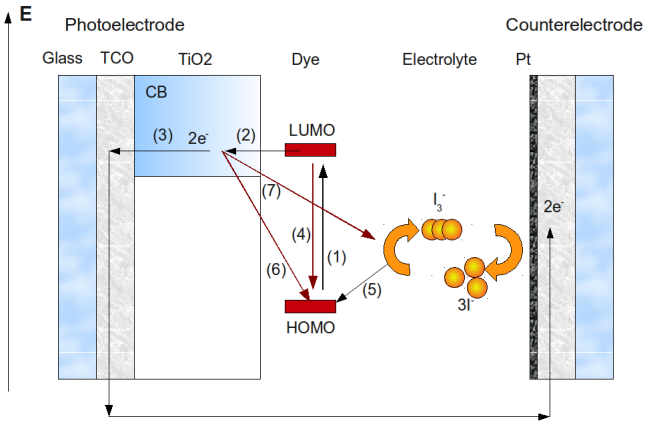

FIGURE 1.2.2. Electron transfer processes in a DSC during light-electric power conversion energy. When the dye absorbs a photon an electron is excited from the HOMO level to the LUMO level of the molecule (1). This is followed by electron injection to the semiconductor (TiO_2) conduction band (2), and the oxidized dye is regenerated by electron capture from the redox electrolyte (5). The injected electron travels by diffusion in the TiO_2 film until it finds it way to the substrate contact where it is released to the external electrical circuit (3). The electron is returned to the cell via an electrolyte reduction reaction at the counter electrode and the electrical circuit of the cell is completed by ionic transport of the redox pair in the electrolyte. The main back-reactions limiting the photocurrent are indicated with red arrows: (4) radiation less relaxation of the excited state of the dye, (6) recombination of the electrons with the oxidized dye, (7) and with the tri-iodide in the electrolyte.

Under illumination, the sensitizer absorbs light and it's photo-excited (1.2.1) with a time scale of few femtoseconds. Then there is the electron injection (1.2.2) from S* to TiO_2, that is a fast process (femtosecond-to-picosecond time scale), accompanied by the electron transport in the photo-electrode (1.2.3). The ground state of the sensitizer is then regenerated by I^- with a microsecond time scale (1.2.5), S^+ could also participate in back-electron transfer reaction from the conduction band of TiO_2 (1.2.6), that happens in the time range from millisecond to microsecond, depending on electron concentration in semiconductor and thus light intensity and usually is prevented by an even faster neutralization of the oxidized dye by the redox electrolyte. Relaxation of the excited sensitized state due to lattice collisions and phonon emissions (1.2.4) is very fast (less then 10 fs) and is a competitor of charge injection. Then there is capture of electron by the oxidized redox specie (1.2.7), that is a slow reaction, until millisecond or second time scale [**27, 4, 28**].
At the photo-electrode the following reaction take place:

(1.2.1) $S|TiO_2 + h\nu \rightarrow S* |TiO_2$ *Light absorption by the dye*

(1.2.2) $S*|TiO_2 \rightarrow S^+|TiO_2 + e^-_{cb}(TiO_2)$ *Charge injection*

(1.2.3) $e^-(TiO_2) \rightarrow e^-(PE)$ *Electron transport*

(1.2.4) $S*|TiO_2 \rightarrow S|TiO_2$ *Relaxation*

(1.2.5) $2S^+|TiO_2 + 3I^- \rightarrow 2S|TiO2 + I_3^-$ *Dye regeneration*

(1.2.6) $S^+|TiO_2 + e^-(TiO_2) \rightarrow S|TiO_2$ *Recombination*

(1.2.7) $e^-(TiO_2) + I_2 \rightarrow I_2^-$ *Back reaction*

Then there is the ionic diffusion in the electrolyte:

(1.2.8) $$3I^-(CE) \rightarrow 3I^-(PE)$$

(1.2.9) $$I_3^-(PE) \rightarrow I_3^-(CE)$$

And the reduction of tri-iodide at the counter electrode:

(1.2.10) $$I_3^-(CE) + 2e^-(CE) \rightarrow 3I^-(CE)$$

1.2.2. DSSCs components.

Photo-electrodes. The photo-anode is usually composed by a nano-structured porous semiconductor on a transparent conductive oxide (TCO) glass [**29, 30**]. The choice to use a porous semiconductor is useful to increase the effective area of the anode, to permit the connecting of a great number of sensitizer molecules. The most efficient material tested until now is titanium dioxide (TiO_2), even if different metal oxide have been reported in literature [**31, 32**].

TiO_2 is a stable, economic and versatile material. It is possible to obtain this semiconductor with different crystal phases: rutile,

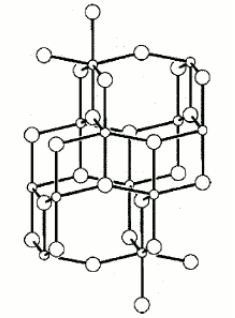

FIGURE 1.2.3. TiO_2 anatase structure.

anatase and brookite. To realize DSSCs electrodes anatase phase is used (figure 1.2.3) [**33**], for it's large band gap, about 3.2 eV, and for the high value of the conduction band edge energy E_c [**34**]. In DSSC the most common titanium oxide nano-structure used is compose by nanoparticles with a size from ten to few hundred of nanometer, even if it is possible to use other structures, such as nonowire or nanorods [**35, 36, 37**] or different deposition techniques [**38**].

After to be excited from sensitizer molecules, electrons are injected into the TiO_2 conduction band, with a time constant (τ_{inj}) that is in the femtosecond-to-picosecond time regime (eq. 1.2.2). Thus, as the electrons traverse the interconnecting network of TiO_2 particles to the transparent charge-collecting back contact TCO, undergoing many trapping and detrapping events [**39, 40, 41**]. An

alternative are the recombination-relaxation processes, discussed in previous section (eq. (1.2.6),(1.2.7), (1.2.4)) [**40**]. To keep neutrality the photoinjected electrons are shielded by electrostatic charges from ions migrated from the electrolyte solution near the surface of the nanoparticles.

The generation collection problem is therefore usually formulated using the 1-D continuity equation [**42, 43**]:

$$\frac{\partial n_c}{\partial t} = \eta_{inj}\alpha(\lambda)I_0 e^{-\alpha(\lambda)x} + D_n\frac{\partial^2 n_c}{\partial x^2} - \frac{n_c - n_{c0}}{\tau_n} \tag{1.2.11}$$

Where $n_c(x,t)$ is the density of electrons in the conduction band of the oxide, $\alpha(\lambda)$ is the absorption coefficient of the dye-sensitized medium at a specific wavelength, n_{inj} is the injection efficiency, I_0 is the incident photon flux corrected for reflection losses at $x = 0$, τ_n is electron life time, D_n is the diffusion coefficient of electrons and n_{c0} is the equilibrium electron density (dark condition). Competition between collection and back reaction of electrons can be expressed in terms of the electron diffusion length

$$L_n = \sqrt{D_n\tau_n} \tag{1.2.12}$$

Efficient electron collection is obtained only if the electron diffusion length exceeds the film thickness [**44**].

The injection of charges by the dye causes an increase in chemical potential of electrons in the semiconductor, this phenomenon, which is the change in potential due to the different concentration of charges, is described by the capacity $C = dQ/dV$ [**45**]. Assuming that the contact between TiO_2 and transparent electrode is reversible, the energy variation of TiO_2 electrons per unit volume in the electrode will be equal to the variation of the Fermi level in the semiconductor:

$$-n_c e dV = dE_{Fn} \tag{1.2.13}$$

Therefore, the capacity per unit of volume in the film will be:

$$C = -e\frac{dn}{dV} = e^2\frac{dn}{d\mu_{Fn}} \tag{1.2.14}$$

Where μ is the chemical potential. The concentration of electrons in the conduction band can be described by the classical Boltzmann distribution law:

(1.2.15) $$n_c = n_0^{(E_{Fn}-E_{F0})/k_BT}$$

If we assume that the conduction band does not move during the accumulation of electrons, the change in the Fermi level depends only on the chemical potential of electrons and the capacitance can be expressed as follows:

(1.2.16) $$C^{cb} = \frac{e^2}{k_BT} n_c = \frac{e^2}{k_BT} n_0^{(E_{Fn}-E_{F0})/k_BT}$$

The electron trapping states in the TiO_2 bandgap are generally approximated by an exponential distribution $g(E)$ depending on energy (eq.) with a tailing parameter T_c. The density of the traps are higher for states energetically near the conduction band but much lower for deep traps that were energetically far away from the conduction band.

(1.2.17) $$C^{tr} = e^2 g(E_F) = \frac{e^2}{k_BT_c} n_{tr0}^{(E_{Fn}-E_{F0})/k_BT_c}$$

The total chemical capacitance of electrons in the DSSC is given by the following equation:

$$C = e^2 \frac{\partial(n_c + n_{tr})}{\partial \mu_n} = C^{cb} + C^{tr} \tag{1.2.18}$$

Chemical capacitance could give information about trapped states in DSSC device, in next section experiment techniques to measure it will be showed.

Main characteristics of a good counter-electrode material are a low charge transfer resistance and a good catalytic skill for the reduction of tri-iodide.The counter electrode (photocatode) is usually a platinized TCO glass, but also carbon material or conductive polymers could be used. Until now best results are obtained using nanoscale platinum clusters, deposited with a thermal treatment of Pt-chloride compounds, on FTO glass [**46, 47**].

Dye. An ideal dye have to absorb solar radiation in all its range of wavelengths starting from 300 nm. Anyway half of the total power of the sun is between 400 to 750 nm, so absorption spectrum of the photosensitizer should cover mainly visible region and even the part of the near-infrared.

The dye must cover the semiconductor with a single layer of molecule, to optimize the charge injection. For this reason it should have anchoring groups to strongly bind the dye onto the photo-anode surface, reacting with hydroxil group of the semiconductor oxide . The most common anchoring group is carboxylic acid (-COOH), that shows a good stability. Different binding modes between carboxylic acid and semiconductor surface are possible: hydrogen bonding, chemical bond formation with a unidentate linkage, a bidentate (or chelating) linkage, or a bridging linkage. The chelating linkage is the one that gives the more interfacial quantum yields of electron injection due to intimate contact between anchored dye and semiconductor surface.[**48**]

An other important requirement is that the excited state level of the photosensitizer should be higher in energy than the conduction band edge of n-type semiconductor, so that an efficient electron transfer process between the excited dye and conduction band of the semiconductor can take place.

Then, to permit the dye regeneration, the oxidized state level of the photosensitizer must be more positive than the redox potential of electrolyte.

The dye exerts its function mainly in two moment: first there is an electronic excitation, then the separation of electron-hole pairs. When the dye absorbs light some electrons shift from the highest occupied molar orbital (HOMO) to the lower un-occupied molar orbital (LUMO). Difference in population between two levels, respect the termal equilibrium situation, gives a difference in chemical energy (Fermi levels):

$$\Delta\mu = \mu_H - \mu_L \tag{1.2.19}$$

In a thermodynamic description, this difference comes from the fact that absorbing species and the source of the incident radiation (in this case the Sun) are at different temperatures, and it's possible to prove that:

$$\Delta\mu = \left(1 - \frac{T_0}{T_s}\right)(\mu_H - \mu_L) \tag{1.2.20}$$

The separation of charges can be made using selective contacts, can be crossed by only one type of charge (electrons or holes), and block the passage of the other. It's possible because the phenomenon of charge transfer depends on the kinetics of the process, both

by the overlapping of energy levels that participate. Therefore, a material with the conduction band close in energy to the excited state absorption of the absorber will be crossed by electrons rather than holes, while the transport of holes will be favored if the energy of the band is close to the sensitizer ground state.

The conversion efficiency of solar energy depends on the amount of electrons which actually pass through the external circuit. The intensity of this current can be determined integrating the conversion efficiency of incident photons in current (IPCE, Incident Photon-to-Current Efficiency) with the solar spectrum under standard AM 1.5 condition. The IPCE is given by:

$$IPCE = LHE(\lambda) \times \eta_{cc} \times \varphi_{inj}$$

where LHE (Light Harvesting Efficiency) is the efficiency of absorption of radiation, and depends on the wavelength, φ_{inj} is the electron injection efficiency and η_{CC} is charge collection efficiency.

Improvement of LHE is a central aspect for DSSC. From the Beer-Lambert law:

$$LHE(\lambda) = 1 - 10^{-\varepsilon(\lambda)LC}$$

where L is the optical length, C the concentration of the dye, and $\varepsilon(\lambda)$ is the molar absorption coefficient of the dye. LHE can be maximized by combining porosity and thickness of the semiconductor, or by choosing a dye with the appropriate ε.

Different photosensitizers have been studied for DSSCs application, including metal complexes, porphyrins, phthalocyanines and metal-free organic dyes. In this thesis two type of dyes are studied: metal complexes and organic metal free dyes.

Metal complexes. Metal complexes and mainly ruthenium (Ru(II)) complexes, are the first dyes investigated for DSCs application because of their broad absorption spectra and favorable photovoltaic properties, such as a long excited-state lifetime and a good electrochemical stability [**49, 50**].

Generally, metal complex photosensitizers consist of a central metal ion with ancillary ligands (typically bipyridines or terpyridines) having at least one anchoring group. Light absorption in the visible part of the solar spectrum is due to a metal to ligand charge transfer (MLCT) process. Anchoring groups have the aim to link the dye with the semiconductor and permit the injection of the excited electron into the conduction band of the semiconductor. The central metal ion is therefore a crucial part of the overall properties

of the complexes. Ancillary ligands can be tuned by different substitutes (alkyl, aryl, hetero-cycle, etc.) to change the photo physical and electro-chemical properties and thus improve the photovoltaic performance.

Most of the dyes used in DSC development have a structure like $Ru(bpy)_2(SCN)_2$, where the two isothiocyanate groups (SCN) cause a shift of the highest occupied molecular orbital from the metal center to them. This permits the visible absorption of the dye by shifting its absorption spectrum to the red.

The groups anchored on the bipyridyl ligands first allow the dye to anchor on the semiconductor surface with an anchoring group, that could be a carboxylate (CO_2^-) or a phosphonate (PO_3^-). Then they have the aim to avoid that dye molecules form a multilayer on the semiconductor substrate, usually alkaly chains are used to reach this scope.

The most famous ruthenium complexes developed for DSSCs are N3, N719 and Z907.

At the beginning in DSSC research, the N3 sensitizer and its salt analogue N719 were developed (Figure 1.2.4a and 1.2.4b). N719 possesses two tert-butylammonium groups to balance the net charge of this compound to zero. Z907 dye (Figure 1.2.4c) is a typical

amphiphilic analogue of N719. When adsorbed on a surface, the two alkyl side chains are positioned in the direction of the surrounding medium and form a barrier to the surface.

Organic dyes. Organic metal-free dyes are simple to synthesized and usually have a higher molar extinction coefficients than those of Ru complexes.

Generally, donor-π-bridge-acceptor (D-π-A) structure (figure 1.2.5) is the common character of these organic dyes [**51**]. When a dye absorbs light, intermolecular charge transfer occurs from subunit D to A through the π-bridge. The injections of electrons from the dye excited stare into the conduction band of the semiconductor, happens trough the electron acceptor group A. Many efforts have been made to change the different parts of organic dyes to optimize DSC performance. In particular the structure of the π-bridge is important to establish the absorption band region [**52**].

Many of these dyes show aggregation problems on semiconductor surface. This problem could be solved modifying sensitizer structure or adding additive in dye solution.

Electrolyte. The redox couple present in the electrolyte has the task of regenerating the ground state of the oxidized dye, and to

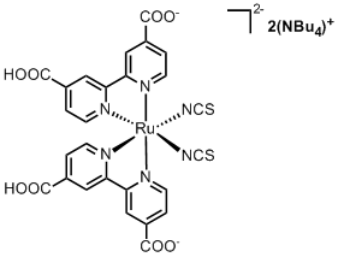

(A) N719

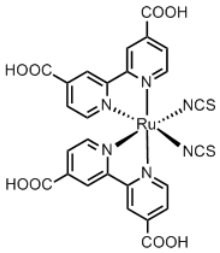

(B) N3

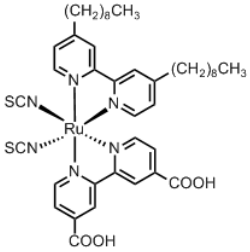

(C) Z907

FIGURE 1.2.4. (a) N719 sensitizer, (b) N3 sensitizer , (c) Z907 sensitizer

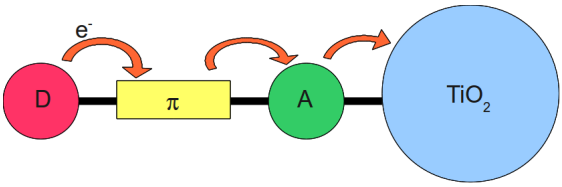

FIGURE 1.2.5. schematic function of D-π-A organic dye for a TiO_2 photo-anode.

transport holes to the counter-electrode. Main proprieties of a good electrolyte are:

- The redox potential must promote the reduction of oxidized dye as fast as possible, to avoid recombination (1.2.6).

- The solution should not significantly absorb in the same range of wavelengths of the photosensitizer, to not limit the cell efficiency.

- The solvent must not cause desorption of the dye from the semiconductor.

- The solution have to allow a rapid diffusion of charge carriers, in particular by a low viscosity.

- A good compatibly with the sealing, to avoid evaporation and cell degradation.

Many additives are used in electrolytes, to change photochemical performances. They affect mainly the redox couple potential, the conductive band of semiconductor and dye regeneration. For

this reason the chemical composition of the electrolyte plays a role in shift the open circuit voltage. In fact, species that do not participate in the conversion of light, such as Li^+ ions or protons, can be adsorbed on the surface of the semiconductor and decrease the Fermi level, lowering V_{OC}. At the same time the presence of cations on the titania surface affect the local iodide concentration, with positive effects on dye regeneration [**53**].
4-tert-Butylpyridine (TBP) shifts the TiO_2 band edge toward higher energy. The opposite effects of TBP and Li^+ make their combination a good additive in DSSCs electrolyte.
An other typical additive is guanidium thiocyanate, that, even if shift the conduction band edge of TiO_2 toward lower energies, increases electron lifetime [**54, 55**].

Liquid redox electrolytes have showed some problems, in particular corrosive problem and evaporating phenomena, that cause cell degradation. In order to avoid these difficulties, recently materials that perform the same function as an electrolyte in solution, but that is state solid, have been studied. These materials are called Hole Transport Materials (HTM), and can be p-type semiconductor, crystalline inorganic salts, molecular solids, or conductive polymers [**56**]. The regeneration of the oxidized state of the dye happened

by the transfer of electrons from the HOMO of HTM, that then is reduced at the counter-electrode. Unlike what happens in a liquid electrolyte, in these cases, charge transport is electronic, not ionic.

CHAPTER 2

DSSCs photo-sensitizers

Two class of dyes were tested, to improve efficiency for DSSCs.

One class is a class of sensitizer was a thiocyanate-free cyclometalated Ru(II) complexes class, in combination with dcbpy-anchoring ligands, 2-phenylpyridine and 2-(2,4-difluorophenyl)pyridine anionic ligands bearing thiophene-based $\pi-$conjugated groups on the pyridine ring. This work was made in collaboration with the University of Milano.

The other class of dye are squaraine-based sensitizers. Squaraine dyes absorb strongly in the NIR spectral region. Usually the absorbance peak in the NIR region is very narrow, for this reason one aim is to enlarge the adsorption band to obtain a strong panchromatic incident IPCE, to improve efficiency. Two different type of squaraine sensitizer were tested, at LPI laboratory, EPFL.

2.1. DSSCs fabrication

In this section is reported the procedure for DSSCs fabrication as performed in Milano Bicocca laboratory. During the work in other institutes a quite different procedure was be used. These differences will be explained in the following sections.

2.1.1. Photo-anode. In order to exclude metal contamination all of the containers are in glass or teflon and are treated with EtOH and 10% HCl prior to use. Plastic spatulas and tweezers are used throughout the procedure.

FTO glass plates [**57**] (Solaronix TCO 22-7, 2.2 mm thickness, 7 $\Omega/\square$) are cleaned in a detergent solution for 30 minutes using an ultrasonic bath, rinsed with pure water and EtOH. Glasses are treated under UV radiation for 20 minutes [**58, 59**]. FTO plates are treated with a freshly prepared 40 mM aqueous solution of $TiCl_4$ for 30 min at 70 °C and the rinsed with water and EtOH [**60, 61**].

A first transparent layer is screen-printed using a transparent TiO_2 paste (Solaronix Ti-Nanoxide T/SP). The coated films are dried at 125 °C for 6 min and then a TiO_2 paste scattering layer is screen-printed. The coated plates are kept in a cabinet for 5 minutes and then thermally treated under an air flow at 125 °C for 6

min, 325 °C for 10 min, 450 °C for 15 min, and 500 °C for 15 min. The heating ramp rate is 5 - 10 °C/min. The sintered layer is treated again with 40 mM aqueous $TiCl_4$ (70 °C for 30 minutes), rinsed with water and EtOH and heated at 500 °C for 30 minutes. After cooling down to 80 °C the TiO_2 coated plate is immersed into a 0.1 mM solution of the dye in EtOH or other solvent, containing 1:1 chenodeoxycholic acid for 20 h at room temperature in the dark. The thickness of the layers, consisting of 11 μm transparent layer and a 5 μm scattering layer, is measured by means of a VEECO Dektak 8 Stylus Profiler.

It's possible to optimize the heat process through a thermogravimetric analysis (TGA), that permit to establish the changes in weight in relation to change in temperature.

When the titania film are ready they appear as a porous film of nanoparticles (figure 2.1.1) [**62**] with a high porosity (>50%).

Using Raman spectroscopy it's possible to check molecular structure of the titania film, and also of the dye up taken.

The Raman spectrum could be obtained on a TiO_2 film coated with the sensitizer and was used to check molecular structure [**63, 64**]. A helium-neon laser (HeNe) was used for Raman spectroscopy at 632.8 nm, while a yttrium aluminum garnet (Nd:YAG) laser was

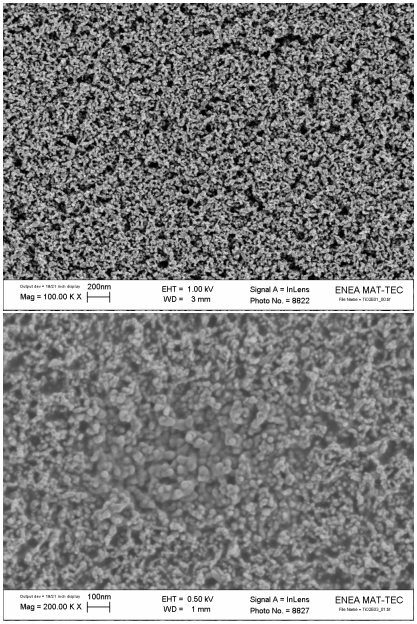

FIGURE 2.1.1. SEM image of a TiO_2 film on FTO glass. Solaronix Ti-Nanoxide HT paste is used. It's possible to observe the porous structure. The pictures are made at the MAC-TEC laboratory of ENEA research center in Rome.

used to obtain resonance Raman spectroscopy at 532 nm. With this technique it is possible to observe the peaks that correspond to the vibrational energy band of TiO_2 anatase structure (table1) and to the sensitizer molecules [**65, 66, 67**].

TABLE 1. The assignment between Raman shift and vibrational energy band is reported.

Raman shift [cm^-1]	Vibrational assigment
400.64	B_{1g} TiO2 Anatase
516.80	A_{1g}+B_{1g} TiO2 Anatase
639.62	E_g TiO2 Anatase

2.1.2. Photocatodes and electrolytes. Counter electrodes were prepared according to the following procedure. A 1 mm hole was made in a FTO plate using diamond drill bits. The electrodes were then cleaned with a detergent solution for 15 minutes using an ultrasonic bath, and then with acetone for 15 minutes again using an ultrasonic bath. After heating at 400 °C for 15 min a drop of a 5 mM solution of H_2PtCl_6 in EtOH (1 mg/mL Pt) was added and the thermal treatment at 400 °C for 15 min repeated. They are then gradually cooled to room temperature.

Figure 2.1.2 shows the SEM image of a counter-electrode realized with this technique.

Most of electrolytes used are iodine-based electrolytes in a mixture of acetonitrile/valeronitrile. Electrolytes were prepared using

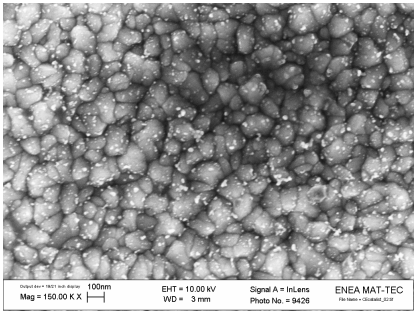

FIGURE 2.1.2. SEM image of a photocatode obtained by thermal decomposition of platinum precursor. It's visible the FTO structure and platinum nanoparticles.

anhydrous solvents. Specific components of each electrolytes will be describe in experimental part of next sections.

2.1.3. Device assembly. Standard DSSC is a sandwich type device. Figure2.1.3 shows assembly processes.

Device sealing is made in a dry box, with a nitrogen flux. As sealing in used a Surlyn® film of thickness 25 μm. A frame is hand cut and it's placed between the two electrodes. Then the system is placed on an hot plate at the temperature of 125 °C and pressed to permit a good sealing. Electrolyte is injected in the cell using the "vacuum back filling" technique. Device is placed in a little essicator and a drop of electrolyte is put on the counter-electrode hole. Then

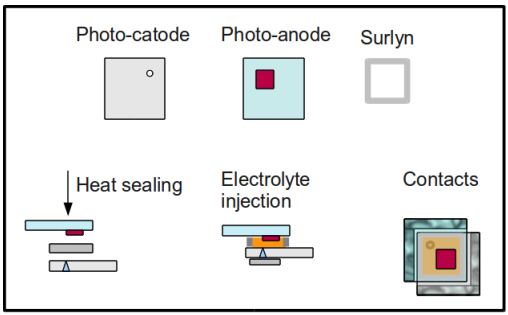

FIGURE 2.1.3. Photo-anode and photocatode are assembled using a Surlyn® frame. On an hot plate the components are heated and pressed. After the electrolyte is injected using vacuum back feeling technique, and then the hole on counter-electrode is closed using Surlyn®. Silver paste is used to make contacts better. A strip in put on the conductive side of each electrodes.

the vacuum is made using a vacuum pump to permit the air to go away from the cell. When the pump is turned off, electrolyte enter in the device. The hole is the sealed using Surlyn® again. When device is ready silver paste is used to improve contact on both electrodes.

2.2. Device characterization

2.2.1. Current voltage characterization. Current-voltage characterization in one of the most important measurements to establish the good work of a solar cell. In fact the power conversion

efficiency of a solar cell depends on the current generated respect to the applied voltage.

I/V characteristic of a solar cell is well described using a diode model [**68**], as showed in figure 2.2.1. In the dark the diode responds to a applied voltage bias (V) with a dark current (I_d), modeled as:

$$I_d = I_s(e^{qV/k_BT} - 1) \tag{2.2.1}$$

where I_s is the reverse saturation current density, $k_B$is the Boltzmann constant, q the electron charge.

Under illumination a photo-current is generated (I_{ph}). For a non-ideal system, the total current of the cell (I_{cell}) can be written as:

$$I_{cell} = I_{ph} - I_s(e^{\frac{-q(Vcell+I_{cell}Rs)}{mk_BT}} - 1) + \frac{V_{cell} + I_{cell}R_s}{R_{sh}} \tag{2.2.2}$$

where m is the ideality factor, R_s is the series resistance, that include the ohmic resistance of cell's components (TCO glass, electrolyte, titania film, ...), while R_{sh} is the shunt resistance, that include recombination processes. Typical I-V characteristic curves in dark and under illumination is showed in figure 2.2.3.

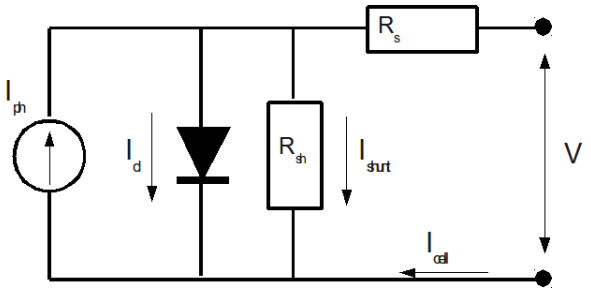

FIGURE 2.2.1. Equivalent circuit for a solar cell.

When $V_{cell} = 0$, short circuit condition, $I_{cell} = I_{sc}$, it's called short circuit current, that is equal to I_{ph} if the resistances are negligible. When circuit is open ($I_{cell} = 0$), $V_{oc} = \frac{mkT}{q} ln(\frac{I_{ph}}{I_s} + 1)$.[**69**]

Effect of series resistance and shunt resistance on I/V device response is showed in figure 2.2.2.

When series resistance increase, there is an decrease in short circuit current density and fill factor decrease. Instead a decrease in shunt resistance causes a decrease in open circuit voltage and a decrease in fill factor too.

Electric-power generated is given by:

$$P_{out} = V\,J \tag{2.2.3}$$

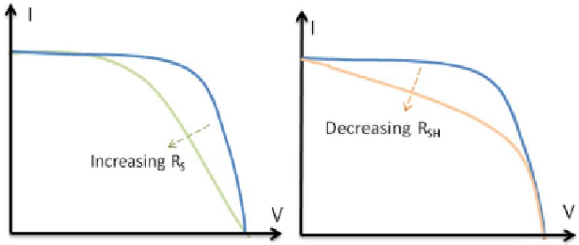

FIGURE 2.2.2. Effect of R_s and R_{sh} on I/V characteristic curve.

where J is the current density. Using the maximum generated power (P_m) is possible to define the Fill Factor (FF) as:

$$FF = \frac{J_m V_m}{J_{sc} V_{oc}} \tag{2.2.4}$$

The efficiency of a solar cell is then described as the ratio between the maximum emitted power and the input power (P_{in}):

$$\eta = \frac{J_m V_m}{P_{in}} = \frac{J_{sc} V_{oc} FF}{P_{in}} \tag{2.2.5}$$

2.2.2. Quantum efficiency. The photocurrent generated by a solar cell under illumination at short circuit is dependent on the incident light spectrum. To relate the photocurrent to the incident

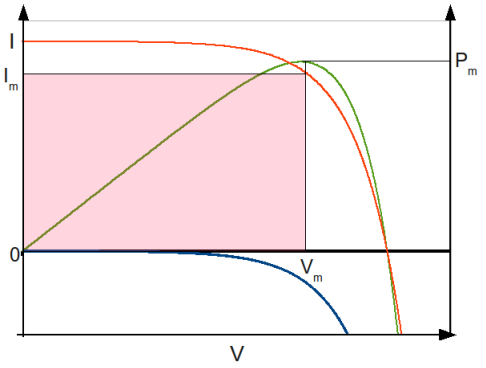

FIGURE 2.2.3. I-V characteristic curves for a solar cell. Red line represents the illumination condition, while the blue line the dark condition. Green line is the emitted power. Light-red area shows the geometrical meaning of FF.

spectrum is useful to use the cell's quantum efficiency (QE), or incident photo to current efficiency (IPCE). IPCE is the probability that an incident photon of energy E will deliver one electron to the external circuit:

$$IPCE(\lambda) = \frac{\#e}{\#\gamma(\lambda)} = \frac{I_{ph}(\lambda)}{\#\gamma(\lambda)/s} = \frac{I_{ph}(\lambda)}{P_{in}} \frac{1240}{\lambda} \tag{2.2.6}$$

It's possible to obtain the photocurrent density (J_{sc}) of a solar cell using:

$$J_{sc} = q \int b(\lambda) IPCE(\lambda) d\lambda \tag{2.2.7}$$

where $b(\lambda)$ is the incident spectral photon flux density.

IPCE depends upon the absorption coefficient of the solar cell material, the efficiency of charge separation and the efficiency of charge collection in the device but does not depend on the incident spectrum. It is therefore a key quantity in describing solar cell performance under different conditions.

Quantum efficiency measurements on DSSCs are usually made superimposing a white light bias on the monochromatic light, to create a constant photocurrent in the cell and to ensure a linear response regime [**70**].

2.2.3. Photo-transient decay measurements. Photo-voltage and photo-current decay measurements are time resolved characterizations, useful to understand time-dependent processes in DSSCs, such as electron recombination and transport, dye regeneration and charge injection [**71, 72**].

Charge density in the TiO_2 layer of a illuminated DSSC could be measured using a open circuit voltage decay measurement. The

device is set to open-circuit condition and then is illuminated with constant white light to produce a steady-state photo-voltage (V_{OC}). When the illumination source is then shut off. The photo-voltage starts to decay due to recombination of free electrons with tri-iodide. After a certain time delay, the cell is short-circuited. The integral of the measured current spike corresponds closely to the remaining charge stored in the film. However, a small fraction of the charge will recombine with tri-iodide during the extraction process. This procedure is repeated with various time delays to obtain the extracted charge as a function of photo-voltage [**73, 74**].

Electron transport and recombination show a nonlinear response to light intensity. For this reason these processes could be studied using small light intensity perturbation superimposed on a larger constant light intensity [**75**]. In this way the photo-voltage decay is a linear function of the total electron density, and the transient response can be fitted with a constant value of the electron lifetime τ_n. In fact the voltage after the application of a short bias shows an exponential behavior:

$$V(t) = V_0 + Ae^{-\frac{\Delta t}{\tau_n}} \tag{2.2.8}$$

where V_0 and A are constant parameters available from fitting data. In analogy to the small perturbation open-circuit voltage transient measurement, it's possible to measure the decay of a perturbed photo-current in short circuit condition. The current decay can be fit using an exponential equation:

$$J(t) = J_0 + Be^{\frac{-\triangle t/}{\tau_c}} \tag{2.2.9}$$

where J_0 and B are fitting coefficients, while the characteristic electron transport time τ_c an be extrapolated from the decay curve, and depends on both the transport and the recombination rate of free electrons at the quasi-Fermi level fixed by the white light bias, according to

$$\tau_c^{-1} = \tau_n^{-1} + \tau_{tr}^{-1} \tag{2.2.10}$$

where τ_{tr} is the electron transport time. In DSSC with iodine electrolyte under short-circuit conditions, the electron lifetime is usually much larger than the electron transport time, so the measured photocurrent response time is nearly equal to the transport time. The

chemical diffusion coefficient, D_n, can be calculated from the electron transport time using:

$$D_n = \frac{d^2}{K\tau_{tr}} \tag{2.2.11}$$

where d is the thickness of the semiconductor film and K is a constant with a value of about 2.5, depending on absorption coefficient of the film.

2.2.4. Impedance spectroscopy. Electrochemical Impedance Spectroscopy (EIS) is an electrochemical technique that consist in a small perturbation of a system by an Alternate Current (AC) signal of low intensity and the observation of the reaction of the system. This approach has the following advantages:

(1) The perturbation has a small amplitude, and this allow that the relationship between current and potential can be considered linear.

(2) Electrochemical impedance spectroscopy gives the possibility to separate the kinetics of the different processes that occur in the system observed in different time scale. On the other hand it is necessary to know how to extract the

data from impedance spectra, and this is often the most complex problem in a EIS analysis. An impedance spectra actually does not tell us anything about the physical consistence of the electrochemical processes that occur in the system examined, it is only by building a physical model that it's possible to extract the properties of the object studied.

In EIS measurements a harmonically modulated small-amplitude voltage $U_{AC} = \triangle U e^{i\omega t}$ is applied, in this way a small AC current $I_{AC} = \triangle I e^{i(\omega t - \phi)}$ flows in the system, with a phase shift ϕ respect the applied voltage U_{AC}. The impedance signal obtain by EIS is:

$$Z_{imp} = \left| \frac{\triangle U}{\triangle I} \right| e^{i\phi} \tag{2.2.12}$$

An EIS measurement can be performed under working condition of the solar cell, under dark condition or under illumination, with different bias imposed. Under open-circuit conditions the modulated small-amplitude voltage U_{AC} is superimposed to the bias voltage

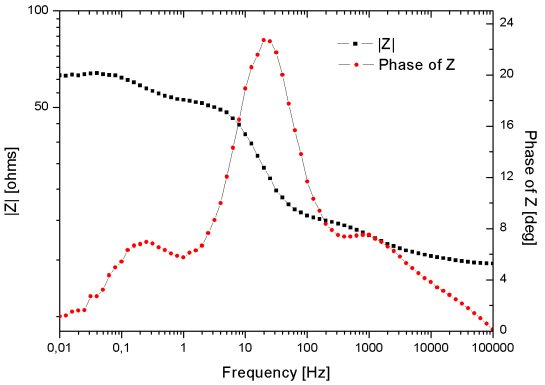

FIGURE 2.2.4. EIS obtained for a DSSC under dark condition with a bias voltage equal to U_{oc}.

U_{oc}. A lot of studies have reported interpretation of impedance spectra, studied different time-dependent parameters. A typical measured EIS spectrum is shown in fig. 2.2.4. Typically three peak are present.

The typical model to interpret this spectra is transmission line model. In this model TiO_2 film is showed as a system of interconnected particles, thought electrons propagated with a resistance r_T, so the total electron transport resistance is $R_T = r_T d$, where d is the film thickness. r_{REC} represents the charge recombination

resistance, due to the recombination of electrons with oxidized electrolyte species at the TiO2/dye/electrolyte interface, while c_μ is the related photo-electrode chemical capacitance; the total interfacial charge recombination resistance is $R_{REC} = r_{REC}/d$ and the chemical capacitance of the film is $C_\mu = c_\mu d$. R_{SU} and C_{SU} are respectively the charge transfer resistance and double layer capacitance at the substrate-electrolyte interface, while R_{CE} and C_{CE} are the charge transfer resistance and double layer capacitance at the counter electrode-electrolyte interface, that represent the regeneration of oxidized iodine at counter electrode. The diffusion of I_3^-/I^- species in liquid electrolyte is described by the diffusion impedance element Z_D . At last R_S is the Ohmic series resistance of the cell, due to resistances of substrate, contacts and electrolyte resistivity.

A more detailed discussion about EIS will be performed in Chapter 5.

2.3. Thiocyanate-free cyclometalated ruthenium sensitizers for solar cells based on hetero-aromatic-substituted 2-arylpyridines

2.3.1. Introduction. The most performing sensitizers to date are 2,2'-bipyridyl (bpy) Ru(II) complexes, such as the most used dye

cis-di(thiocyanato)bis(bpy-4,4'-dicarboxylate) ruthenium(II) (N3 and N719, see section 1.2.2). More recently heteroleptic ruthenium complexes have been investigated, where one of the two bpy-4,4'-dicarboxylate (dcbpy) anchoring ligands has been replaced by a functionalized ancillary (bpy) ligand carrying two electronrich aromatic conjugated substituents on the 4,4' positions of the bpy core [**76, 77, 78**],. In particular thiophene-based substituents led to tunable optical and energetic properties by inducing bathochromic and hyperchromic effects, which resulted in enhanced light-harvesting capacities, higher external quantum efficiencies, improved device photocurrents, and top-ranked power conversion efficiencies [**79**]. On the basis of these distinct and superior characteristics, Grätzel and others referred to these compounds as "supersensitizers". [**80**]

A main drawback of these Ru(II) complexes is the presence of the thiocyanate -NCS ligand. Thiocyanate coordinates through only one atom, which makes easier the replacement by other competing ligands yielding less efficient species, and its coordination to metal ions requires purification steps in order to separate the active N- from the inactive S-coordinated isomer [**81**]. Unfortunately, previous efforts to replace NCS by other ligands such as halides or cyanide always yielded much lower energy conversion efficiencies.

Recently, Nazeeruddin, Graetzel and coworkers have described the cyclometalated ruthenium complex where the thiocyanate ligands have been replaced by the deprotonated form of 2-(2,4-difluorophenyl)-pyridine. This sensitizer is the first reported thiocyanate-free Ru(II) complex showing power conversion efficiencies of approximately 10%. These type of ligands have been widely investigated in cyclometalated Ir(III) complexes mainly for organic light-emitting diodes (OLEDs) thanks to their strong photoemissive properties, but also in nonlinear optics and, more recently, in DSCs [**82, 83, 84, 85, 86**].

On the basis of the enhanced photophysical and photovoltaic properties exhibited by the supersensitizers based on thiophene-substituted bpy ancillary ligands, we were interested in checking whether 2-phenylpyridine and 2-(2,4-difluorophenyl)-pyridine derivatives carrying thiophene-based conjugated substituents on the position 4 of the azine ring could provide a new class of cyclometalated Ru(II) complexes with tunable photophysical, electronic, and photovoltaic properties. Indeed, cyclometalated has been shown to be an important tool for significantly perturbating the optical and electronic properties of the corresponding complexes [**87, 88**].

Rather surprisingly cyclometalated complexes carrying 4-(heteroaromatic-substituted)-2-arylpyridines have never been described in the literature. Cyclometalated Ru-complexes with unsubstituted 2-phenylpyridine or substituted with simple electron-withdrawing substituents on the phenyl ring of the anionic ligand have been very recently described by Berlinguette et al., who demonstrated the relevant effects of the conjugated groups on the electrochemical and optical properties and HOMO/LUMO energies [**89, 90**]. In literature have been recently reported two families of thiophene-based 2-arylpyridines ligands, where the pyridine ring of the new compounds is substituted in position 4 with π-conjugated electron-rich and electron-poor thiophene-based fragments in order to tune optical and energetic properties [**91**]. Indeed absorption/emission, redox features, and HOMO/LUMO energy levels data have demonstrated that the photophysical and electronic properties of the ligands may be tuned over a broad range. Here will be presented an unprecedented class of thiocyanate-free cyclometalated Ru(II) complexes containing, in combination with dcbpy anchoring ligands, 2-phenylpyridine and 2-(2,4-difluorophenyl)-pyridine anionic ligands bearing thiophene-based π-conjugated groups on the pyridine ring. The investigated cyclometalated complexes are collected in figure

2.3.1, together with the corresponding species containing the unsubstituted 2-phenylpyridine (Ph-Py) and 2-(2,4-difluorophenyl)-pyridine (FPh-Py) ligands. The new complexes have been investigated in their optical and electronic properties and DFT/TDDFT calculations have been performed in relation to their substitution pattern. DSCs containing the complexes as photosensitizers have been prepared and photovoltaic properties measured in comparison with reference species.

2.3.2. Optical proprieties. The Uv/Vis absorption spectra of the ligands studied were first performed (figure 2.3.2).

It is evident a red shift of the main peaks and an enlargement of the adsorbance energy band. Considering the fluorine-free ligand, the addiction of one thiophene group causes a shift of the low energy peak from 276 nm to 310 nm and an increase in the molar absorptivity from 8289 $M^{-1}cm^{-1}$ to 15500 $M^{-1}cm^{-1}$. Instead the peak at high energy shows a shift until 262 nm and appears visible, with a molar absorptivity of 15433 $M^{-1}cm^{-1}$. The ligand **Ph-Py-TT** shows a further red shift of the low energy peak, which maximum shifts to 367 nm, with a molar absorptivity about 24200 $M^{-1}cm^{-1}$, while the high energy peak has a blue shift until 255, with an increase in extinction coefficient until 20194 $M^{-1}cm^{-1}$.

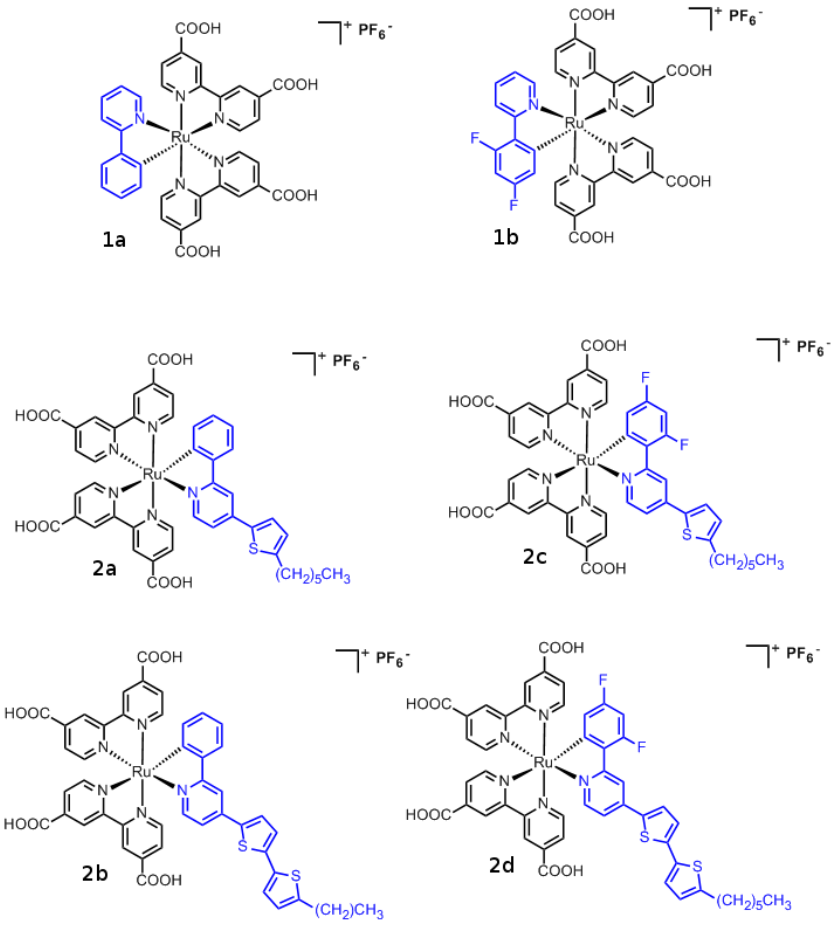

FIGURE 2.3.1. Structures of the cyclometalated Ru(II) investigated in this work (2a-d) and reference literature compounds (1a and 1b).

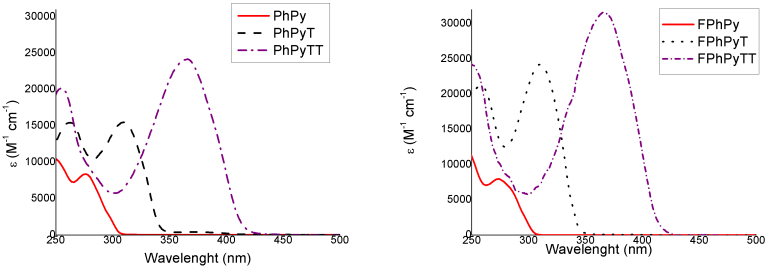

FIGURE 2.3.2. UV/Vis spectra of ligands. On the left the fluorine-free ligands, on the right the analogues with fluorine.

The addiction of fluorine does not cause a substantial peaks shift, but mainly increases the molar absorptivity. Ligand **FPh-Py-T** shows two peaks at 257 nm (21184 $M^{-1}cm^{-1}$) and at 310 nm (24200 $M^{-1}cm^{-1}$). At least the maximum in extinction coefficient is reached by **FPh-Py-TT** low energy peak (31600 $M^{-1}cm^{-1}$). The integrated spectra area increases a lot becoming more than 10 times greater for **FPh-Py-TT** respect that for **Ph-Py**.

The absorption spectra of the cyclometalated complexes **2a–d** in ethanol solutions, along with those of the reference systems **1a** and **1b**, are depicted in figure 2.3.3, while the main photophysical parameters in EtOH are collected in Table 2.

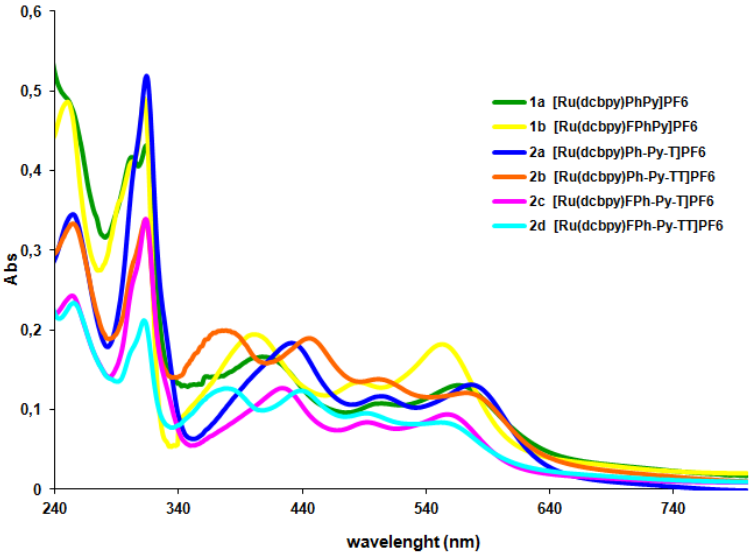

FIGURE 2.3.3. Absorption spectra of the cyclometalated Ru(II) complexes **1a-b** and **2a-d**.

Similarly to unsubstituted complexes **1a** and **1b**, the new complexes with one thiophene substituent **2a** and **2c** present three bands in the visible region due to MLCT transitions. These peaks are blue-shifted upon fluorine substitution on the phenyl ring atoms, in agreement with an increase of the HOMO-LUMO gap. Such blue-shift is particularly significant for the MLCT transition at lower energy, with a 22 nm shift recorded on going from **2a** to **2c**. Besides, comparison of the absorption spectra of **1a** and **1b** with **2a**

TABLE 2. Absorption Parameters of the The New Cyclometalated Complexes **2a-d**, in comparison with reference cyclometalated complexes **1a-b** (EtOH). [a] Molar extinction coefficient ε [10^4 M^{-1} cm^{-1}] in parentheses. [b] The ε value could not been determined due to the low solubility in EtOH.

♯	Complex	λ_{max} [nm][a]
1a	$[Ru(dcbpy)_2(Ph\text{-}Py)]PF_6$[b]	247, 302, 314, 408, 499, 566
1b	$[Ru(dcbpy)_2(FPh\text{-}Py)]PF_6$	250, 312, 402, 485, 553
		(2.2), (2.3), (0.9), (0.6), (0.8)
2a	$[Ru(dcbpy)_2(Ph\text{-}Py\text{-}T)]PF_6$	254, 315 , 432 , 505 , 579
		(3.4), (5.1), (1.8), (1.2), (1.3)
2b	$[Ru(dcbpy)_2(Ph\text{-}Py\text{-}TT)]PF_6$	255 , 314 , 381, 444, 505, 576
		(3.3), (3.3), (2.0), (1.9), (1.4), (1.2)
2c	$[Ru(dcbpy)_2(FPh\text{-}Py\text{-}T)]PF_6$	253, 313, 424, 492, 557
		(2.4), (3.4), (1.3), (0.8), (0.9)
2d	$[Ru(dcbpy)_2(FPh\text{-}Py\text{-}TT)]PF_6$	255, 314, 379, 438, 494, 557
		(2.2), (2.0), (1.2), (1.1), (0.9), (0.8)

and **2c**, respectively, shows that the introduction of the thiophene substituent causes a red shift of the visible bands. When a second thiophene ring is introduced, as in **2b** and **2d**, the two bands at lower energies are almost unvaried, but a red-shift is recorded for the band centered around 430 nm and a new band at about 380 nm appears. Again, a blue-shift is observed on going from **2b** to the corresponding fluorinated complex **2d**. All of the complexes are characterized by high molar extinction coefficients.

2.3.3. Electrochemical proprieties. Electrochemical proprieties were studied by Cyclic Voltammetry (CV) and Differential Pulse Voltammetry (DPV).

Both voltammetries were performed in 0.1 M tetra-butylammonium hexafluorophosphate (TBAPF6) in DMF, at 50 mV/s, using an auger pin electrode. Results show a reversible oxidation and a irreversible reduction.

From oxidative DPV it is possible to deduce for all samples that the oxidation potential is about -0.2 V versus ferrocene. This entails that the HOMO value is about -5.0 eV.

The reductive DPV gives for all samples a reductive potential about -1.25/-1.30 V versus ferrocene, with a corresponding LUMO level about -3.9 eV versus vacuum.

Anyway for more detailed information about electrochemical proprieties computational analysis would be useful.

2.3.4. Photovoltaic performances. The devices were prepared similar as described in section 2.1, with a difference in photoanodes realization. In fact preliminary results were obtained before that the group owned a screen-printing machine. So TiO_2 paste was handily applied using a glass rod and 3M Magic tape to create the film thickness. This method allows to obtain fairly good results,

even if a low reproducibility of outcomes pointed out the necessity to repeat the measurements with screen-printed samples. 0.1 mM solution of the dyes in EtOH containing 1:1 chenodeoxycholic acid were used for photoanodes.

Three different electrolyte solutions were used: A6141 (0.6 M N-butyl-N-methyl imidazolium iodide, 0.03 M I_2, 0.10 M guanidinium thiocyanate, and 0.5 M 4-t-butylpyridine in acetonitrile/valeronitrile 85:15), A6986 (0.6 M N-butyl-N-methylimidazolium iodide, 0.05 M I_2, 0.1 M LiI, and 0.05 M 4-t-butylpyridine in acetonitrile/valeronitrile 85:15), and VT1 (0.6 M N-butyl-N-methylimidazolium iodide, 0.05 M I_2, 0.1 M LiI, and 0.45 M 4-t-butylpyridine in acetonitrile/valeronitrile 85:15) [**46, 92, 93**]. Electrolyte A6986 differ from A6141 for the presence of LiI, absence of the thiocyanate salt, and reduced amounts of 4-t-butylpyridine. The addition of LiI should lead to higher photocurrents, but lower cell photo-voltage, due to adsorption of Li cations onto the TiO_2 surface charging it positively, and thus shifting down its Fermi level. On the other hand the addition of 4-t-butylpyridine to the electrolyte in A6141 raises the conduction band edge of the TiO_2, yielding higher open-circuit voltages, and reduces the recombination of electrons from the semiconductor to the oxidized electrolyte (dark current) through the coordination between

the pyridine nitrogen atom and the Ti sites. The electrolyte VT1 was used in order to combine the beneficial effects of the presence of LiI and 4-t-butylpyridine. DSCs based on N719 and using the standard electrolyte A6141 were investigated under the same experimental conditions as a reference system [**94, 95**].

Photovoltaic measurements of DSCs were carried out using a 300 W Xenon light source (Oriel Solar Simulator 81150). The power of the simulated light was calibrated to AM 1.5 (100 mW cm^{-2}) using a reference Si photodiode. I–V curves were obtained by applying an external bias to the cell and measuring the generated photocurrent with a Keithley model 2400 digital source meter.

Devices were prepared using also reference cyclometalated complexes and N719 dye. N719 dye gave 7.3% efficiency, 15.0 mA/cm^2 J_{sc}, a V_{OC} about 763 and a fill factor about 0.64.
Results are showed in table 3.

It is evident how the complexes **2c** and **2d** show an increase in photovoltaic performances respect the references complexes **1a** and **1b**, that makes them two promising sensitizers. They exhibit in general an increase both in open circuit voltage than in short circuit current density. Then in **2c** sensitizer it is clear the effect of electrolyte additives on V_{OC} and J_{sc}. In fact A6141 electrolyte

TABLE 3. Main photovoltaic parameters of DSSCs based on the new cyclometalated complexes **2a-d**, in comparison with reference cyclometalated complexes **1a-b.**

♯	Complex	Electrolyte	J_{sc}	V_{OC}	FF	Eff.%
1a	$[Ru(dcbpy)_2(Ph\text{-}Py)]PF_6$ [b]	A6141	6.1	484	0.50	1.5
		A6986	6.5	470	0.55	1.7
		VT1	8.6	507	0.55	2.4
1b	$[Ru(dcbpy)_2(FPh\text{-}Py)]PF_6$	A6141	8.0	567	0.62	2.8
2a	$[Ru(dcbpy)_2(Ph\text{-}Py\text{-}T)]PF_6$	A6141	4.2	451	0.49	0.9
		A6986	5.4	441	0.58	1.4
		VT1	5.4	486	0.53	1.4
2b	$[Ru(dcbpy)_2(Ph\text{-}Py\text{-}TT)]PF_6$	A6141	13.1	562	0.40	2.9
		A6986	15.2	479	0.56	4.1
		VT1	11.2	508	0.64	3.6
2c	$[Ru(dcbpy)_2(FPh\text{-}Py\text{-}T)]PF_6$	A6141	9.4	615	0.65	3.8
		A6986	11.8	552	0.63	4.1
		VT1	12.4	597	0.62	4.6
2d	$[Ru(dcbpy)_2(FPh\text{-}Py\text{-}TT)]PF_6$	A6141	11.9	617	0.67	4.9
		A6986	16.4	532	0.50	4.4
		VT1	14.6	561	0.49	4.0

allows to reach the highest V_{OC}, while VT1 the highest J_{sc}, and also the highest efficiency. Electrolytes effects are not so clear for other sensitizers. **2d** dye has the best efficiency, near to 5%, with A6141 electrolytes, and it also has the best open circuit voltage. **2b** dye exhibits the best efficiency (4.1%), with electrolyte A6986, that allows to reach the highest current density for this dye, even if the open circuit voltage is relative low (479 mV). **2a** dye shows a low

efficiency (lower respect to the reference dyes), due mainly to low current density.

Preliminary results are encouraging to continue the study on these complexes, especially for their potential high current density. New measurements will perform soon to analyze in details dyes proprieties.

2.4. A Near Ideal Panchromatic Response in DSCs with a Squaraine Sensitizer

2.4.1. Introduction. The record efficient squaraine dye in literature is YR6 dye, with an efficiency of 6.7%, that shows a good panchromatic IPCE (>50%) from 450-700 nm [**96, 97, 98, 99**]. The basic idea is modify YR6 molecule structure to synthesize a squaraine dye with further extended conjugation through an elongated π-bridge, trying to obtain:

1) a bathochromic shift of the main absorption peak

2) strengthening high-energy absorbance bands.

To improve the IPCE of YR6 sensitizer a larger π-system with a cyclopentyldithiophene (CPDT) bridge was included in place of

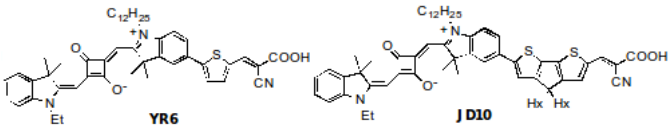

FIGURE 2.4.1. YR6 and JD10 dyes. A thiophene is substituted with a CPDT bridge.

thiophene (Figure 2.4.1). CPDT could significantly contribute to increasing the absorbance of high-energy absorption bands, contributing in this way in increasing the photocurrent. Furthermore, the electron-rich character of CPDT could induce a bathochromic shift when compared to thiophene through narrowing the optical band gap, $E^{(0,0)}$, by destabilizing the ground rate redox potential (S^+/S) predominately.[**100, 101**]

2.4.2. Optical proprieties. The UV/Vis/NIR absorption spectra of JD10 and YR6 solutions in ethanol were measured. Figure 2.4.2 shows the molar absorptivity obtained. JD10 sensitizer shows a maximum absorbance peak at 672 nm, with a red shift respect the maximum obtained for YR6. Even if the extinction coefficient of this peak is of 175,000 $M^{-1}cm^{-1}$, about 40% lower respect the value obtained for YR6 (279,000 $M^{-1}cm^{-1}$), the absorption peaks are considerably broadened compared to YR6 dye. It is also evident

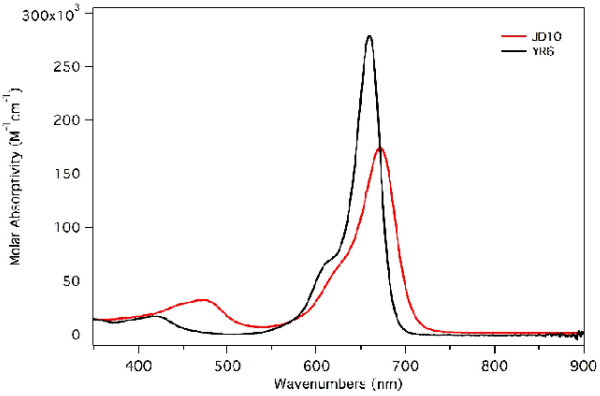

FIGURE 2.4.2. UV/Vis/NIR absorption spectrum of JD10 compared with YR6 one. It's possible to observe the peak at 474 nm.

a high-energy transition due to the CPDT bridge at 474 nm with a molar absorptivity of 33,000 $M^{-1}cm^{-1}$, a good result if compared with the minimal absorbance of 2,000 $M^{-1}cm^{-1}$ observed with YR6 in this region. Finally JD10 sensitizer absorbs strongly in to the NIR region until 728 nm with a molar absorptivity always higher of 5000 $M^{-1}cm^{-1}$. As result of these consideration, the integrated area of JD10 absorption curve shows only a 20% decreasing respect YR6.

The optical density was measured for 2.8 μm thickness TiO_2-coated films with JD10 dye and compared with YR6 coated films

(Figure 2.4.3). Different solutions were used, with different chenodeoxicholic acid (CDCA), to test the aggregation phenomena.
A broadening of the absorption spectrum peaks was observed for films of JD10 as had been previously noted for YR6. It is important to observe how the optical density measurements indicate only a 9% decrease for JD10-sensitized TiO_2 films compared with YR6 films of the same thickness at their respective absorbance maximum, while in EtOH solution the difference between the molar extinction coefficients of JD10 and YR6 was about 40%. This phenomena suggests a significantly higher dye-loading for JD10 to explain the big change in percent between the film optical densities and solution molar absorptivity.

From optical density graph is then possible to observe the aggregation problem. JD10 dye shows a strong aggregation peak at 630 nm on TiO_2 films which is only observable in the solution absorbance as a slight shoulder. The addiction of CDCA cause a reduction of the aggregation peak at 630 nm for JD10 as can be seen from the film optical density measurements. At the same time there is a strong reduction in optical density intensity for all wavelengths. YR6 dye has been previously shown to have an optimal CDCA loading of 10

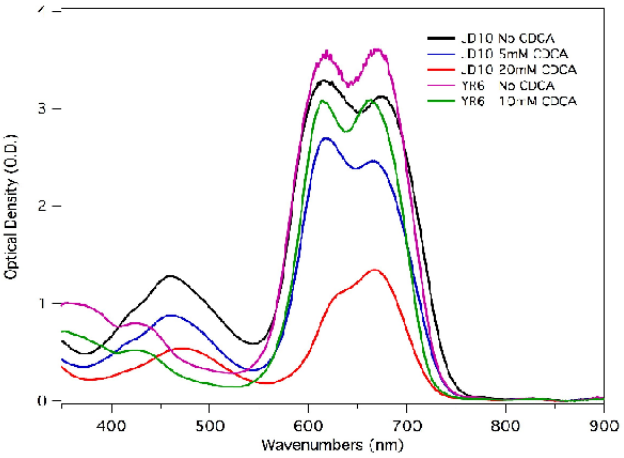

FIGURE 2.4.3. Optical density of sensitized 2.8 μm TiO2 films prepared by immersion in a solution of 0.1 mM JD10 without CDCA, 0.1 mM JD10 with 5 mM CDCA , 0.1 mM JD10 with 20 mM CDCA , 0.1 mM YR6 without CDCA and 0.1 mM YR6 with 10 mM CDCA in ethanol for 14hours.

mM for DSSCs, however no obvious change in the aggregation peak intensity (610 nm) is observed at this loading.

2.4.3. Photovoltaic proprieties. Standard sandwich-type solar cells were realized to test this dye.

As working electrodes a double layer TiO_2 film (8 μm of active transparent layer and a 5 μm of a scattering layer) on a Nippon sheet glasses with a resistance of 10 $\Omega/\square$ were used. The counter

electrodes were platinized TCO glass with a resistance of 15 Ω/sq, Electrolyte was the JH34 electrolyte, a redox iodine based electrolyte (0.6 M DMII, 0.05 LiI, 0.03 M I_2, 0.05 M guadinimium thiocyanate, 0.25 4-t-butylpyridine in acetonitrile/valeronitrile 85:15). The anode was dipped in a 0.05 mM solution of dye in ethanol for 16-20 hours. At the beginning of the study different concentrations of CDCA in dye solution were tested, to check the effect on photovoltaic performances. Best results were obtained using 20 mM CDCA concentration, in agreement with optical density measurements consideration. Devices were measured using a mask with an active area of 0.185 cm^2.

At 1 Sun illumination (AM 1.5G) the device with JD10 as sensitizer gave a short-circuit photocurrent density of 16.4 mA/cm^2, an open-circuit voltage of 635 mV, and a fill factor of 0.70, that give an efficiency of 7.30 %.

This efficiency is about 10% higher respect previous results obtained in literature with YR6, this improvement is mainly due to increase in the photocurrent (figure 2.4.4). This is evident also by the increase in IPCE over the same broad range of wavelengths (Figure 2.4.5).

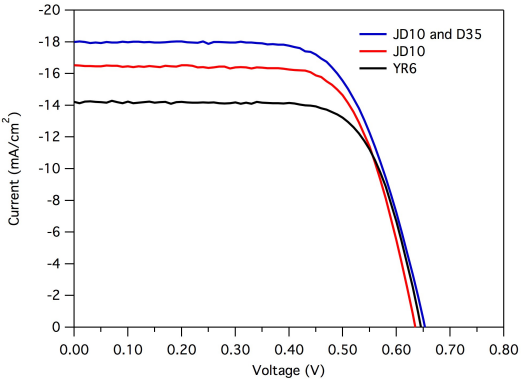

FIGURE 2.4.4. Current-voltage characteristics for cells obtained using JD10, YR6 and D35 dyes. The most evident difference is in short circuit current density.

It is possible further improve efficiency, getting better absorbance in low wavelengths region. For this reason was realized a device with JD10 dye co-sensitized with D35 sensitizer (figure 2.4.6)[**102, 103**]. Figure 2.4.7 shows the optical density of a 2.8 μm thickness TiO_2 film sensitized with JD10, JD10:D35 and D35. It's possible to observe how the presence of D35 dye both increase the peak at high energy, and decrease the peak at low energy. Than it appears that the JD10 aggregation shoulder in low energy peak decreases with D35 co-sensitization, in fact D35 sensitizer has a de-aggregating function.

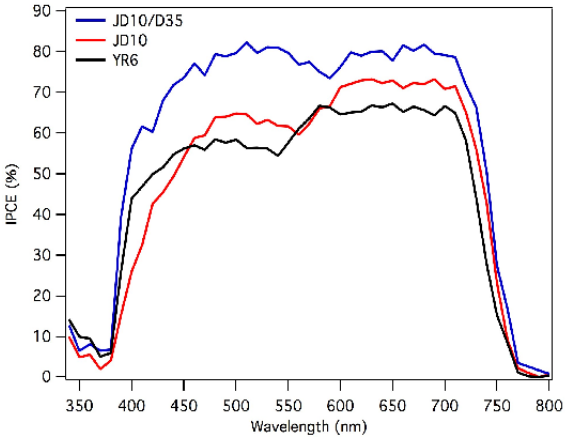

FIGURE 2.4.5. IPCE curves for cells obtained using JD10, YR6 and D35 dyes.

IPCE of this solar cell (Figure 2.4.5) in very flat between 400 to 750 nm, near to a panchromatic-shape IPCE. In particular is interesting to observe that there is an increase in IPCE intensity, respect the JD10 device, not only in the D35 absorbance area (400-550 nm), but also in all other regions. The reason of this panchromatic shape IPCE is clear by observing optical density. In fact the effect of D35 dye in contrast JD10 aggregation allows the IPCE to increase also in high energy region, where there is not absorbance by D35 sensitizer.

Co-sensitized solar cell, measured in standard condition, gave a photocurrent density of 18.0 mA/cm^2, an open circuit voltage of 653

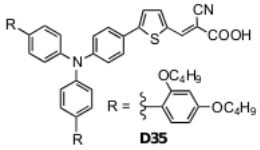

FIGURE 2.4.6. D35 dye structure

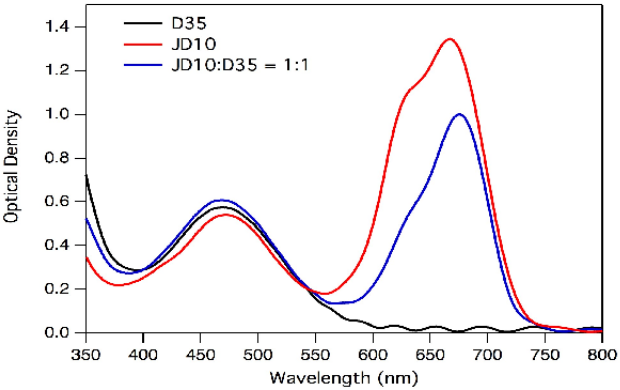

FIGURE 2.4.7. Optical density for D35, JD10 and D35:JD10 dyes. Effect of co-sensitization is evident in high energy region.

mV, and a fill factor of 0.67, with a total efficiency of 7.90%. The photocurrent obtained is the highest value obtained in literature for a squaraine dye by either single metal-free organic dye or its co-sensitization with other organic dyes. Respect solar cells obtained using only JD10 dye there is an increase in current density and only a little increase in open circuit voltage.

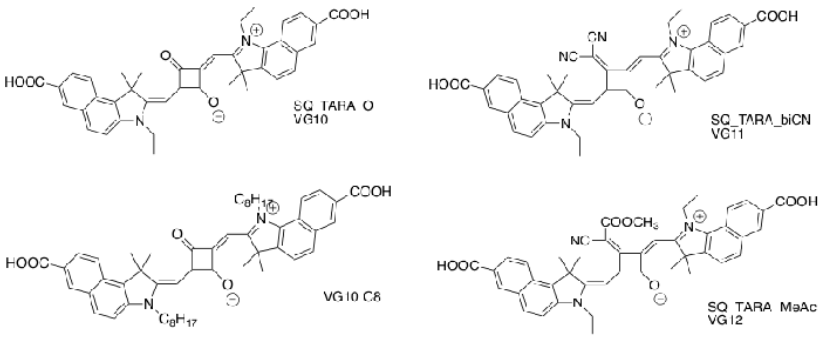

FIGURE 2.5.1. VG10, VG11, VG12 and VG10-C8 dyes.

2.5. A high-Efficiency and Stable Symmetrical Panchromatic Squaraine for Dye-Sensitized Solar Cells

2.5.1. Introduction. In this section the study on photovoltaic performances of four different bis(benzoindoline) squaraine dyes is presented. Studied sensitizers are showed in figure 2.5.1.

These dyes have a symmetrical structure. Some modification are made on VG10 dye, adding different functional groups, to modify HOMO level. VG10-C8 chain presents a long added chain, to avoid aggregation phenomena.

One of the first studies symmetrical and unsymmetrical performances of squaraine dyes in DSSCs was made by Das and coworkers [**104**], who characterized a series of both symmetric and un-symmetric squaraine dyes possessing a nonconjugated -COOH grafting group enabling the stable anchoring of the dye on the titania surface. They found that the sensitization efficiencies of unsymmetrical squaraines in DSSCs are significantly higher than those of symmetrical squaraines, and ascribed this to a unidirectional flow of electrons on excitation of unsymmetrical squaraines whereas increase in charge density towards the center of the molecule was observed for the symmetrical squaraines. Properly designed nonsymmetric squaraines show a somewhat directional HOMO–LUMO excitation. It has been shown that the absorption of self assembled dyes on TiO_2 can be efficiently converted into a photocurrent only in the presence of a directional HOMO–LUMO excitation providing a charge displacement from a region distant from the surface (in the ground state) to the surface close proximity (in the excited state) [**105, 106**].

Later works by Burke and Grätzel demonstrated that even symmetric squaraines can efficiently perform, as long as the dye is absorbed as the corresponding ammonium salt and in the presence of

chenodeoxycholic acid in order to prevent dye aggregation at the surface[**107**].

Until now, the most efficient symmetrical squaraine dye was SQ1 which has demonstrated the evident advantages of using symmetrical structures in synthesis process [**108**].

Analyzed VG10 series sensitizers present similar structure but have more extended conjugation than SQ1. These dyes incorporate a directly attached carboxylic acid on both the benzoindoline instead of having it in the N-alkyl substituents. These two squaraines are quite similar to the unsymmetrical SQ02 which presented one benzoindoline moiety without any carboxylic acid [**109, 110**].

2.5.2. Optical proprieties. Optical density was measured using a 2.8 μm thickness TiO_2film. All dyes were measured in solution with or without cheno-deoxycholic acid, to analyze aggregation effect (figure 2.5.2). Only the solution without CDCA or with 10 mM CDCA (maximum concentration used) are there analyzed.

VG10 sensitizer shows the higher adsorbance, but also a strong aggregation peak at low energy, at about 630 nm. The addiction of CDCA (10 mM) causes a decrease in this peak and in general a decrease in optical density. The main absorption peak has a decrease more than about 30% and the total integrated area becomes quite

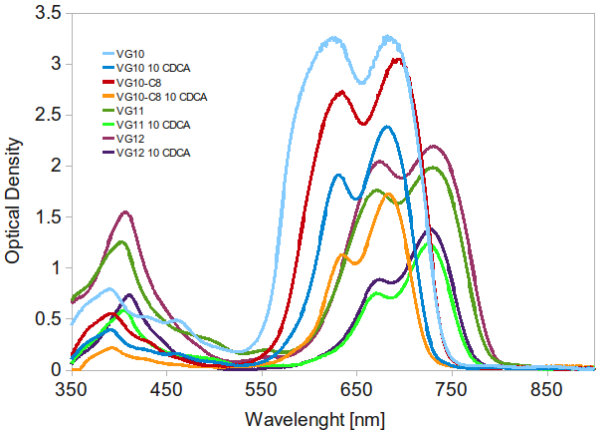

FIGURE 2.5.2. Optical density of VG10, VG11, VG12 and VG10-C8 dyes, with different concentration of CDCA. Measurements were performed on 2.8 μm thickness TiO_2 films.

an half.

VG10-C8 sensitizer has an optical response similar to VG10. It shows a lower aggregation peak, explicable by the introduction of the long chains in molecular structure. Also in this case the addiction of CDCA cause a reduction in optical density intensity, in particular the aggregation peak, still visible, is subject to a great reduction respect the main peak. Total area of optical density, in the presence of CDCA, becomes quite an half the total area of VG10 optical density in the same conditions.

VG11 and VG12 sensitizers show similar shape optical density spectra. In general the absorptivity is lower . Then it is possible to observe a bathochromic effect that cause a shift of the main peak until 725 nm. Also in this case it is evident the effect of CDCA on aggregation peaks and also on optical density.

2.5.3. Photovoltaic characteristics. All dyes have been studied in standard sandwich type devices.

Effect of CDCA on photovoltaic performances was tested first on VG10 dye. Working electrodes were 4 x 4 mm square shape transparent TiO_2 films, 3.1 μm thickness on NSG 10 $\Omega/\square$ glass, electrolyte was JH34 (section 2.4.3). Standard platinized FTO glasses were used as counter electrode. Results are reported in table 4. adding CDCA there is an increasing in efficiency mainly due to the increase in open circuit voltage. With 10 mM CDCA concentration there is a great increase in voltage, but at the same time a decrease in current density, probably due to the competitive adsorption between the CDCA and the dye on the TiO_2 sites.

Figure 2.5.3 reports IPCE measurements performed by these devices. It is evident how the addiction of CDCA cause an increasing in IPCE both at low and high energy.

TABLE 4. Effect of CDCA in VG10 solution in THF. Three different CDCA concentration were tested. Data reported refer to fresh devices and 1 day old devices.

	Eff %		V_{OC} [mV]		J_{sc} [mA/cm^2]		FF	
	Fresh	1 day	Fresh	1 day	Fresh	1 day	Fresh	1 day
VG10 0 CDCA	3.33	2.17	519	513	9.45	6.72	0.68	0.63
VG10 1 CDCA	3.45	2.52	566	570	9.14	7.04	0.67	0.63
VG10 5 CDCA	3.91	3.25	589	598	10.06	8.61	0.66	0.63
VG10 10 CDCA	3.91	3.51	639	654	8.78	7.88	0.70	0.68

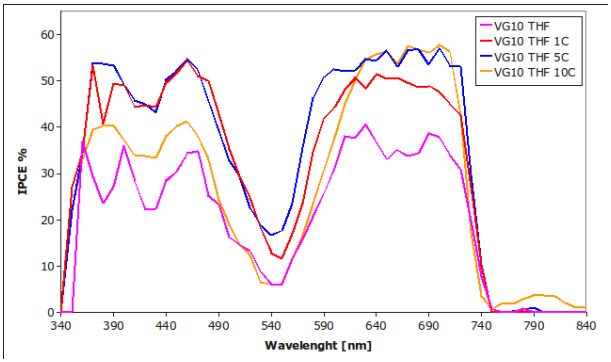

FIGURE 2.5.3. IPCE measurements on devices reported in table 4. Effect of CDCA addiction is evident in the spectra shape and in IPCE increasing at low energy.

It is interesting to note how there is a degradation for devices after one day.

JH163 electrolyte was tested. It has the same composition of JH34,

TABLE 5. Photovoltaic results for squaraine dyes in the optimized device conditions. For VG10 and VG10-C8 dyes, different concentrations of CDCA are reported. For each dye are reported data of the fresh cell end the 1 day old cell with anti-reflective layer.

	Eff %		Voc [mV]		Jsc [mA/cm^2]		FF	
	Fresh	1 day	Fresh	1 day	Fresh	1 day	Fresh	1 day
VG10 0C	2.77	3.11	533	544	7.82	8.57	0.67	0.67
VG10 2.5C	4.97	5.57	597	619	13.10	14.13	0.64	0.64
VG10 10C	5.22	5.54	605	612	13.64	14.35	0.63	0.63
VG11 10C	3.02	3.42	562	582	7.35	9.10	0.73	0.65
VG12 10C	3.48	3.47	592	601	8.51	8.48	0.69	0.68
VG10C8 0C	2.68	3.28	560	585	7.73	8.81	0.62	0.64
VG10C8 2.5C	5.30	5.65	608	623	13.19	13.67	0.66	0.67
VG10C8 5C	4.82	5.03	604	618	11.79	11.97	0.67	0.68
VG10C8 10C	5.38	5.64	611	628	13.35	13.51	0.66	0.66

with also CDCA inside. For this study working electrodes used were compo double layers TiO_2 (8 μm active layer and 5 μm scattering layer). Dye solutions were prepared with different CDCA concentration. Table 5 shows results obtained for all dyes.

For all sensitizers there is an increase in performances after 1 day, differently for what previously observed. VG11 and VG12 dyes have the lower efficiency, respectively about 3.42% and 3.47%, caused mainly by the low photo-current (figure 2.5.4). VG10 and VG10-C8 show similar parameter at the same concentration of CDCA, and

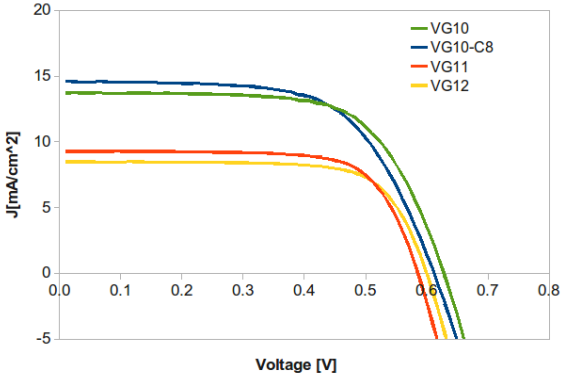

FIGURE 2.5.4. I/V characteristic curves for optimized devices for all dyes.

both of them reach an efficiency over 5%. From figure 2.5.5 it is possible to observe how the higher IPCE value obtained by VG10-C8 at low energy is compensated by a broader VG10 peak at high energy. The result is that two dyes have almost the same current density.

For these two sensitizes different concentrations of CDCA are reported. In fact it is interesting to note how without CDCA the open circuit voltage of devices obtained with VG10 and VG10-C8 have a great difference, about 40 mV, while adding 10 mM CDCA, the difference in open circuit voltage becomes lower, about 16 mV.

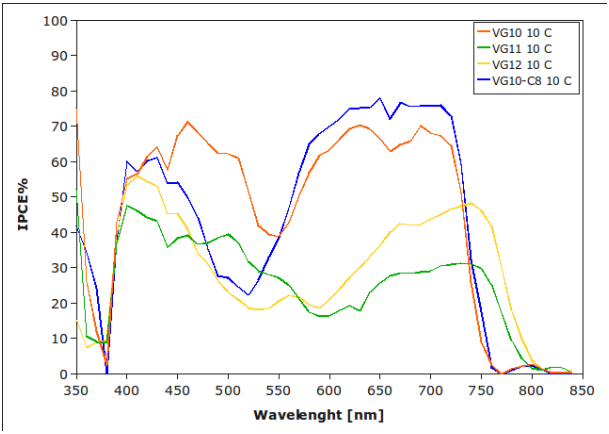

FIGURE 2.5.5. IPCE curves obtained for optimized devices.

Photovoltage transient measurements were made to explain this behavior . Figure reports open circuit voltage and voltage decay as a function of capacitance obtained for studied devices.

One preliminary analysis points out as at a certain capacitance value, devices without CDCA exhibit a higher difference in voltage respect devices with an high concentration of CDCA. This phenomena could explain the open circuit trend observed.

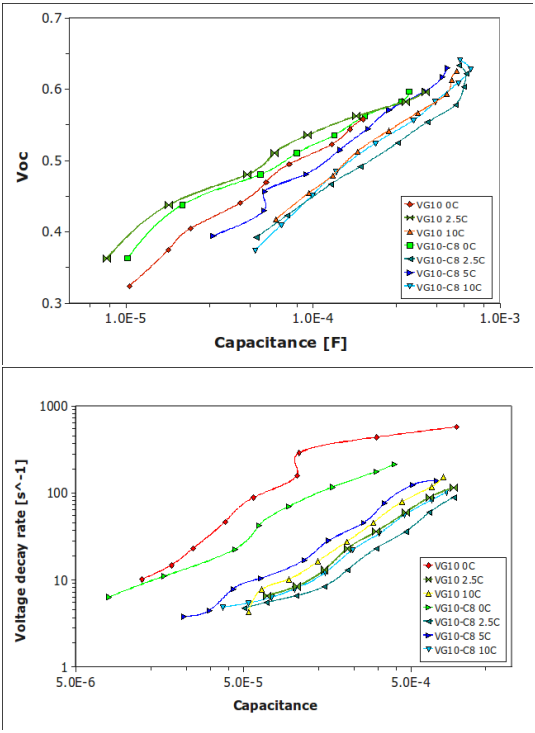

FIGURE 2.5.6. Open circuit voltage and voltage decay rate as a function of capacitance for VG10 and VG10-C8 dyes at different CDCA concentrations.

2.6. Conclusion

Two different class of sensitizers were studied, analyzing main proprieties. Different diagnostic techniques were performed to understand how optimize the devices and the capability of the dyes.

The study on cyclometalated ruthenium sensitizers is in phase of conclusion, anyway preliminary results are very encouraging and make possible to suppose that final results will show high photovoltaic performances. In particular an high photocurrent and a broaden IPCE are expected.

Study on JD10 sensitizer allowed to obtain a flat and panchromatic IPCE, with a high efficiency for a squaraine dye. This sensitizer showed a record efficiency and a useful application in co-sensitization with organic-dye.

At last the study of modifications on VG10 dye structure permits to observe the effects of these changes and to obtain an high efficiency symmetric squaraine dye.

CHAPTER 3

Spectroscopic evaluation of dyeloadig on TiO_2

3.1. Introduction and state of art

One of the major problem in DSSC fabrication is lack of reproducibility. Device production a sequence of different steps, and many variables could compete in affect final result. As a consequence, the fabrication of a DSSC is often based on the meticulous repetition of reported protocols, but the influence of e great variability make difficult to evaluate unequivocally the real performance of new material tested. From a point of view of a possible industrialization process, the optimization and reproducibility of any step is very important.

Dye-loading process is topically a long process (about 20 hours for most sensitizers). The long time request for dye-loading is due essentially to ensure a complete absorption from the substrate. A few studies have reported a strong effect of different dye dipping time on the photovoltaic performance of the cells.[**76**] This in turn

derives from the magnitude (amount of adsorbed dye on TiO_2 surface) and from the kinetic of the adsorption process [**111, 112**]. To this concern, the effective loading of the dye in the TiO_2 electrode is of paramount relevance for controlling, and eventually optimizing, photovoltaic cell parameters. In particular, current density is directly proportional to the light harvesting ability of the dye sensitizer, which is related to the dye concentration on TiO_2 surface (1.1.2) [**113**]. Moreover it is also proved as the dye adsorption behavior directly affects the cell open-circuit voltage.[**114**]

Indirect ex-situ surface coverage studies based on dye adsorption/desorption process represent the most common tool: the amount of adsorbed dye is determined by desorbing the dye from the TiO_2 surface by treating with an aqueous or alcoholic solution of NaOH and then measuring the desorbed dye concentration by spectroscopy in the ultraviolet-visible (UV-Vis) spectral range.[**115, 116**]

A similar, alternative method has also been proposed [**117**], based on the measurement of diffuse reflectance on the dyed TiO_2, then calibrated with the amount of dye desorbed after a proper treatment, measured by UV-Vis absorption; such an approach may represent a tool for studying the dye adsorption process, described in terms of characteristic parameters such as the adsorption and

desorption rate constants and the number of adsorption sites available on the TiO_2 surface. The above techniques have the advantage of allowing a quantitative determination of dye loading, but it is time-consuming and it presents inherently indirect method, since the measurement is not carried out on the adsorbed dye, so one has to trust on the reliability of the extraction procedure and on the stability of the dye and on its optical response when adsorbed and desorbed. For these reasons, it cannot represent a fast and reliable methodology for routine dye loading measurements.

More recently, a new method for a quantitative estimate of the adsorbed dye has been proposed, based on photo-electron spectroscopy [**118**]. Nonetheless, it presents strong limitations to a wide use: first, it is destructive and not easily available; in addition, it gives only the relative concentrations of different elements, then used to indirectly determine the amount of adsorbed molecules. Considering direct methods, different authors also proposed non-destructive techniques, particularly meaningful since they can be applied in-situ, during adsorption of the dye on the TiO_2 surface [**119, 120**]. Watson and coworkers performed the analysis by monitoring the color intensity during dye uptake as well as by measuring diffuse reflectance. Getting in-situ information is particularly useful when interested in

time-evolution of the process, which is observed to follow a characteristic time dependence, which varies with film thickness and dye. Nonetheless, both techniques need a transparent photoanode substrate, which represents a serious limitation, can work only at a few wavelengths, and cannot separate the dye signal detected from the adsorbing film or from the native solution. The data from both techniques are also used to get absolute dye concentrations, which can be one of the relevant goal of such analysis, but only after desorption and independent quantitative dye estimate.

An alternative in-situ method was proposed by Peic and coworkers and is based on attenuated total reflection at the interface between the dye solution and the TiO_2 film. It gives the total amount of adsorbed dye, after proper calibration through desorption, but it is applicable only after the ad hoc deposition of a metallic film; finally, it works at a fixed wavelength. The work is particularly interesting, although not fully convincing, when it discusses the dying mechanisms and dying evolution in time.

As for the description of the adsorption mechanisms, an interesting approach, which nonetheless does not deal with a quantitative evaluation of the dye concentration, is the combined use of several spectroscopies, as proposed years ago by Leon and coworkers

[**121**]; such an approach was not used any longer, possibly because it requires several different measurements, some of them requiring specific electrodes.

A few studies have focused attention on the kinetic of the dye up-taking process. Concina and coworkers have very recently compared N719 loading kinetics on TiO_2 photoanodes under continuous flow conditions and static impregnation, showing that the latter process provides better dye up-taking [**111**]. Here an in situ UV-Vis real-time monitoring has been proposed although quantitative measurements were taken at one single wavelength of the dye spectrum. It should be noted that in this, and other works, different adsorption process phases, a rapid initial dye uptake followed by a slower adsorbed dye increase, have been evidenced. This effect has been rationalized in terms of a rapid surface adsorption and a simultaneous slower mass transfer process (dye diffusion through the solution to the TiO_2 nano-particle and percolation of the dye through the porous film).[**122**]

Park et al. have measured the amount of adsorbed dye on TiO_2 surface as a function of immersion time of the semiconductor film in the dye solution finding a pseudo- first order adsorption kinetics.

Once again, the adsorbed dye was quantitatively determined from the absorbance at a single wavelength (510 nm).

For what concerns direct non destructive *in-situ* methods, different techniques have been proposed in literature. Some of them are based on UV/Vis measurements, that use a single wavelength signal to relate the change in adsorption intensity to dye-loading on semiconductor film. In this chapter I present a measurement method which consists of measuring the UV-Vis optical spectra of TiO_2 electrode films after different treatments in a prototypical dye solution, then calibrating the absorption intensity with the desorbed dye absorption. This protocol has some advantages respect ones analyzed in literature. First we used a spectroscopic technique, that allows to record the absorption spectra over a wide wavelength range, not only a fix energy beam. In this way it is possible to obtain a more detailed information about peak intensity, also in the case in which a peak shift is observed. Than the use of several samples would allow to relate optical density of TiO_2 film with desorbed dye solution, to find out the amount of dye molecules on semiconductor film. In this way it is possible to obtain a sort of calibration for each dye, to estimate the optimum dye-loading process. In the last part the kinetic process of dye-loading will be analyzed.

3.2. Materials and instruments

To realize the samples FTO-coated glass plates (2.2 mm thick, resistance 7 ohm/□ purchased from Solaronix) were used as substrates. A glass was cleaned as reported in 2.1. No treatment with $TiCl_4$ was performed to avoid to alter optical proprieties of glass. The TiO_2 paste (Ti-Nanoxide Solaronix, particle size about 15-20 nm) was screen-printed (section 2.1) using a mesh that permit to obtain about 2.5 μm thickness layer for this kind of paste. Two TiO_2-film layers are been printed to obtain TiO_2 films have a square shape of dimension 4x4 mm, with a rough surface, and a thickness of 5.0 - 5.5 μm. A set of 16 samples were prepared for this study. Optical measurements on bare TiO_2 films were made to check the good reproducibility of the sample. In fact big differences in films optical proprieties could make results less reliable..

Each sample was immersed into 4 ml of a solution of N719 in EtOH (0.5 mM) in the dark and in the air for a specific period of time, then rinsed with acetonitrile and dried under a nitrogen stream. A set of 16 samples with different dye-uptake time (from 5 seconds to 24 hours) has been prepared and submitted to spectroscopic investigation.

After the spectroscopic investigation on the dye-sensitized films, the dye was desorbed using 4 ml of a 0.1 M solution of NaOH in ethanol/H_2O (1:1) and the adsorption spectra of these solution were be measured.

Comparison with spectra of freshly prepared solutions of the dye in the same solvent, at known concentrations, could to be used to determine the amounts of desorbed dye.

Optical measurements were performed using a Perkin-Elmer spectrometer Lambda900. Measurements on the films have been performed in transmission configuration at normal incidence in the spectral range 300 $\div$ 2000 nm. A light spot size of about 3 mm^2 has been used for collecting transmitted light from the middle of the dye-coated film. Due to the reduced thickness of the substrate and the size of semiconductor nanoparticles, the effect of the stray-light due to the diffuse reflectance of the TiO_2 film can be considered negligible. Thus, absorption spectra of the dye-coated films have been corrected with the optical response of the bare TiO_2 films. Transmission measurements of dye-desorbed solutions have been performed by using the same spectrometer in the spectral range 200 $\div$ 800 nm.

3.3. Results

3.3.1. Preliminary results. As described in the previous section samples were prepared using a screen-printing machine. Anyway a preliminary study was made before that this machine would be available from the research group. The study has two different strategies: first a set of samples were measured as previously described, then a single sample was dipped in the dye solution several times, increasing in this way the total dipping time.

For these measurements the samples were prepared in a similar way respect what described in the previous section. The difference is the deposition of TiO_2 paste. This is printed by a "doctor-blade" technique, using a 3M Magic tape to determine the film thickness and a gloss rod to spread the paste. The film obtained with this technique had a thickness about variable between 11 to 15 μm. Unlikely this thickness was not uniform and the film surface was not flat, but showed irregular regions. The sample has been cut to make 25 samples of dimensions 2.0 x 2.0 cm.

Optical proprieties of these films have been studied. Figure 3.3.1 shows transmittance measurements performed on the same sample

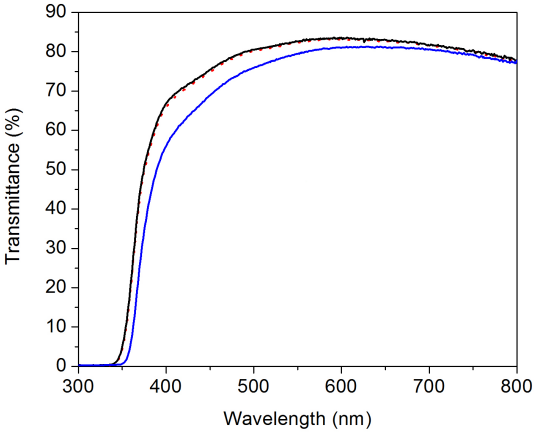

FIGURE 3.3.1. Transmittance performed on the same sample in three different regions. Two regions (black and red dotted lines) show a good agreement, while the last region has a lower transmittance, that suggests a thicker TiO_2 film.

in different region. Results pointed out the great variability of substrates and the necessity to select a defined region to perform measurements, to avoid that surface irregularities affect the results.

Figure 3.3.2 reports the transmittance of some of the the analyzed samples. These data will be used to normalize the optical data obtained on the dye-coated films, showed in figure 3.3.3.

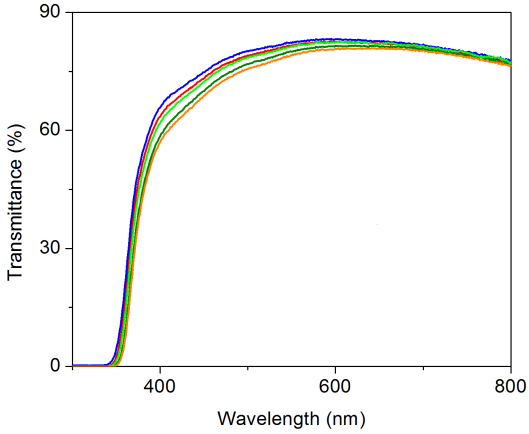

FIGURE 3.3.2. Transmittance performed on bare TiO_2 films.

The shorter dipping time (5 seconds) already shows a change in sample optical response respect bare substrate. The two characteristic peaks of N719 appear at about 400 and 540 nm. Peaks intensity increases increasing dipping time, but some unexpected behaviors are present. The spectra corresponding to 5 and 8 hours dipping time overlap themself, like the spectra corresponding to 3 and 6 hours. Then it is not possible to observe a saturation in dye -loading.

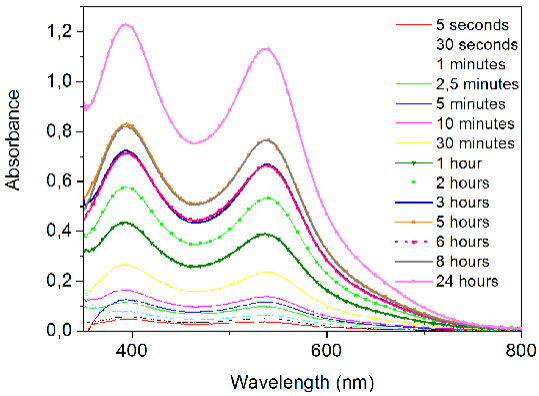

FIGURE 3.3.3. Absorption spectra obtained for dye-coated TiO_2 film. Samples dipping times vary between 5 seconds to 24 hours.

All these problems are clearly related to the differences in films thickness, that change the kinetics of the process and could not be simply removed by a substrate normalization.

To ride out this problem the same measurements were repeated using only a sample, dipped several time in dye solution to obtain increasing dipping time. From figure 3.3.4 it is immediately clear as absorbance intensity increases in a monotonous way, and there is saturation-like behavior. This phenomena is particularly clear in figure 3.3.5, that shows the integration of the spectra from 460 nm

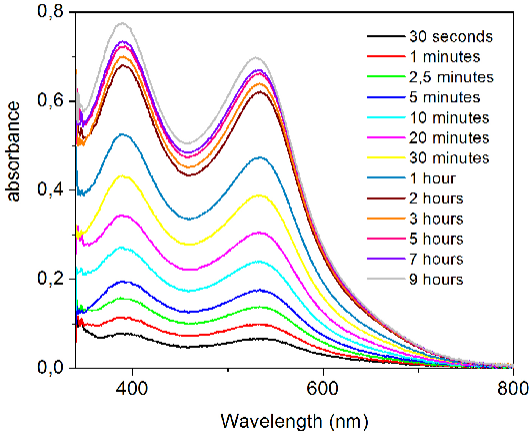

FIGURE 3.3.4. Adsorbance spectra obtained for the same sample at different dipping times, normalized at the bare TiO_2 substrate.

to 800 nm. It is important to point out the shift of the peak at 540 nm in the 9 hours dipping time spectrum. This depends by dye molecules aggregation on TiO_2 surface, that could be dependent from dipping technique. Then we have not any information about change in kinetics of adsorbance process due to a "multi-step" dipping technique.

The results obtained point out the necessity to repeat the measurements using different samples with reproducible morphologies.

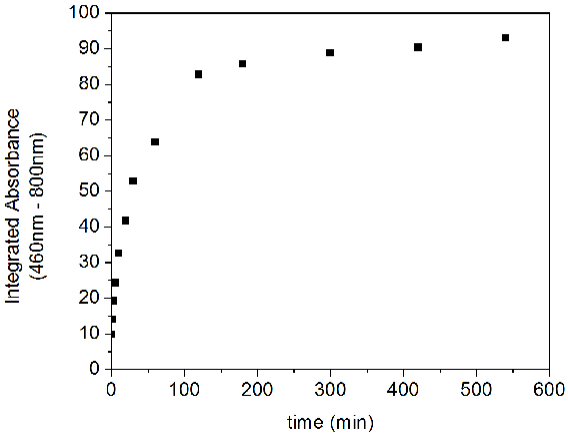

FIGURE 3.3.5. Integrated area of adsorbance spectra showed in figure 3.3.4. Areas increase in a monotous way, but a complete saturation is not reached.

For this reason the experiment was repeated using screen-printed TiO_2 films. Results will be reported in next section.

3.3.2. Optical measurements. Optical measurements on bare TiO_2 film were performed. A typical spectrum shape is showed in figure 3.3.6.

The transmittance is high, reaching 75%, in the visible and near infrared spectral range. The long spectral range used (until 2000 nm) allows to observe interference fringes. Since the thickness of the film

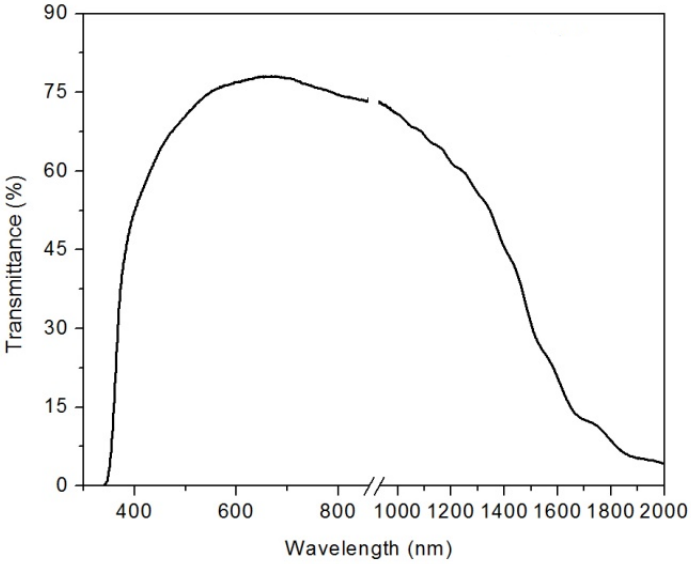

FIGURE 3.3.6. Transmission spectrum of a sample of bare TiO_2 film on FTO glass. In the visible range the transmittance is about 75%, and starts to decrease after 1000 nm. At high wavelengths interference fringes are visible.

was measured using a mechanical profilometer, it is possible to use these information to estimate the refractive index of the mesoporus semiconductor film.

Some papers [**123**][**124**] have reported an analysis of mesoporus film conductor using ellipsometry. In particular from refractive index it is possible to have information about film porosity. The determination of refractive index a porous medium is not so accurate. Anyway it could be an useful tool if another technique is not available. One if the main parameter that penalizes this method is obviously the roughness of the film.

Transmission measurements have been performed on all the TiO_2 films before and after dye-uptaking; for each sample, the spectrum collected before dying was used for normalizing the one collected after dying. The mentioned thickness uniformity over the probed area ensures a variability of the transmittance of the untreated substrates lower than 1.5% (as evaluated at 700 nm) within the whole set, allowing us to consider all of the substrates as equivalent within this accuracy. Finally, transmission measurements of dye-desorbed solutions have been performed by using the same spectrometer in the spectral range $200 \div 800$ nm, with an optical path of 10 mm.

Figure 3.3.7 shows the optical response of the N719 dye adsorbed into the TiO_2 film after correction to the bare substrate (without dye) for a number of selected dipping times.

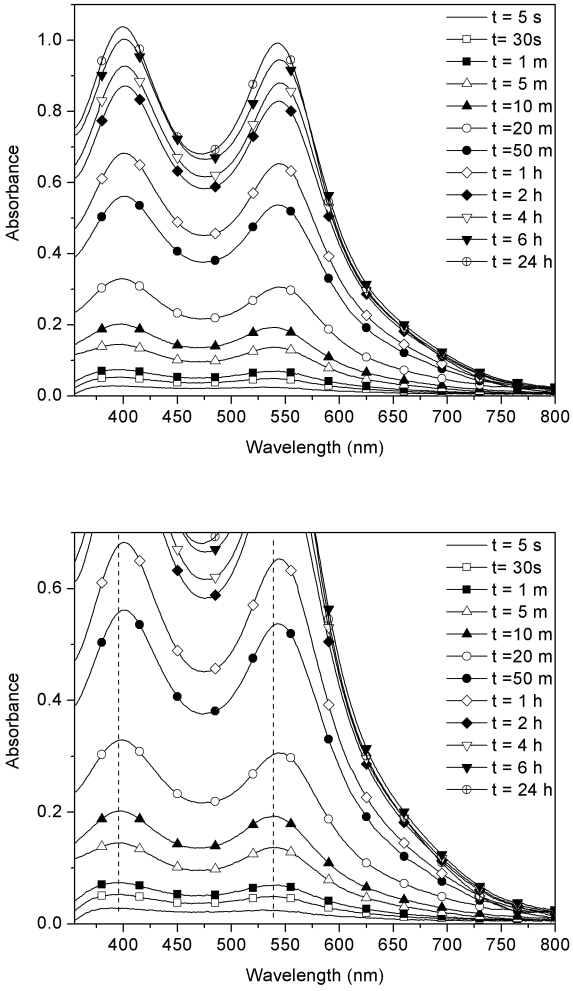

FIGURE 3.3.7. Optical responses for some of studied samples. On the right an enlargement makes the peak shift more evident.

According to the spectrum of N719 in EtOH solution [**49**]-[**35**], the optical signature of N719 dye can be detected at about 540 and 400 nm for all of the different dipping times. A shoulder on the low energy tail of the former peak can be clearly detected at about 650 nm, regardless of the used contact time. The two main bands in the near UV and Vis region are ascribed to $t_2 \rightarrow p^*$ metal-to-ligand charge transfer transitions, and are common to bipyridine based DSC Ru(II) complexes. The effect of the adsorption into the TiO_2 layer is a bathochromic shift of the MLCT band, with the low energy main peak shifting from 530 nm in EtOH to 539 nm in the film, according to literature. The shoulder at low energy was recently computed to be ascribed to a singlet-singlet transition at 649 nm mainly described by the HOMO-LUMO orbital excitation [**125**].

It is worth noting that the spectral line-shape does not significantly vary over the different contact times, event for the shortest times, for which a significant change in intensity was recorded. The relative intensity of the peaks is indeed almost unvaried. The most striking feature is that the spectral position of the peaks slightly changes as the dipping time increases. In particular, the main peaks at 540 and 395 nm show a red-shift to 544 and 400 nm, respectively,

for dipping times higher than 10 minutes. This behavior can be either due to aggregation phenomena of dye molecules on TiO_2 surface, which are more important as the dye loading increases, or to a partial protonation of N719, as the dye interacts with the TiO_2 surface. This clearly demonstrates that performing a single wavelength measurement, even under a real-time monitoring of dye uptaking, might lead to a misinterpretation of spectroscopic data and, thus, partially incorrect quantitative conclusions.

In order to quantitatively determine the amount of adsorbed dye, N719 has been completely desorbed from the TiO_2 films by treatment with with 0.1 M NaOH in H_2O/EtOH (1:1). The solutions of the desorbed dye have been then measured by means of UV-Vis absorption spectroscopy. Figure 3.3.8 shows the absorption spectra of the solutions of desorbed dye as a function of the dipping time of the original samples. The optical response is characterized by the presence of three distinct peaks centered at about 510, 380, and 310 nm. The former two peaks correspond to the MLCT bands, whereas the high energy peak in the UV region is due to $\pi \rightarrow \pi*$ intraligand transitions. As for the spectra of the dye-coated TiO_2 films, a shoulder on the long wavelength tail of the low energy peak can be recorded at about 600 nm. We also note that, once again

similarly to dye-adsorbed films, the spectral position of the peak at about 510 nm slightly varies with the contact time, albeit in this case the spectral position of the other peaks remains almost unchanged. More precisely, the low energy peak is centered at 505 nm at low concentrations of the dye and undergoes a red-shift to 512 nm for higher concentrations, corresponding to dipping times longer than 20 minutes.

In contrast with the spectra of the dye onto the TiO_2 surface clearly in this case, due to the alkaline hydroalcholic medium, we have to rule out the hypothesis that the bathochromic shift at higher concentrations could be due to protonation equilibrium, being all of the carboxylic functionalists present as deprotonated carboxylate COO-. Therefore, dye aggregation is more likely the reason for such shift.

3.3.3. Adsorption kinetics. Kinetic process of dye-loading could be expressed with the following expression:

$$S + TiO_2 \leftrightarrow TiO_2 : S \tag{3.3.1}$$

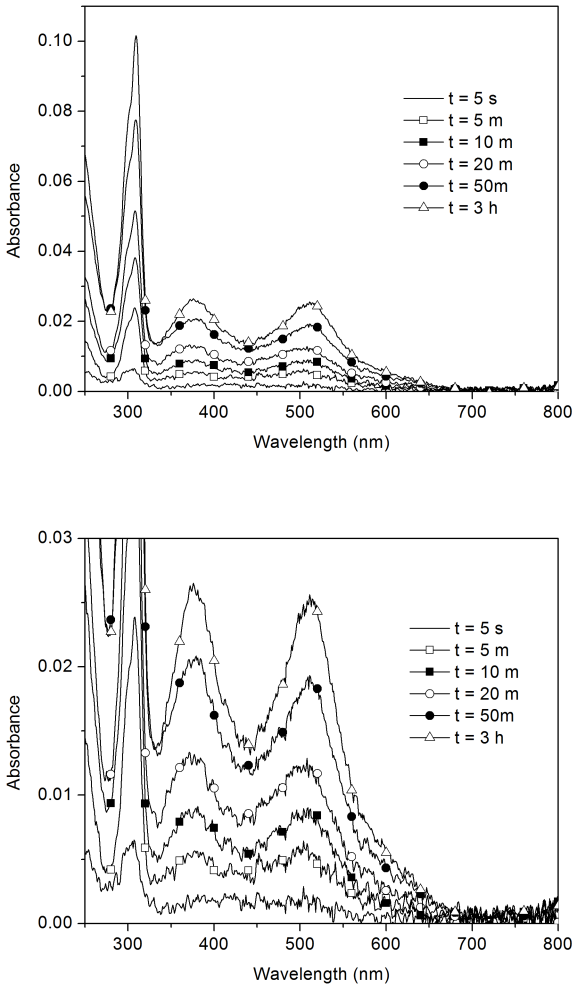

FIGURE 3.3.8. Absorption spectra of NaOH solutions used to dye desorbing. On the right an enlargement allows to observe peaks shift.

where S represents the sensitizer molecules, TiO_2 the titanium dioxide sites available for dye adsorption, and $TiO_2 : S$ represents the semiconductor sites coated by dye molecules. In the studied case the back reaction could be considered negligible, because it is very slow if compared with direct reaction. This assumption is proved by the fact that a N179-coated film immersed in a bath of pure solvent does not color it.

The kinetics of dye loading has been discussed in literature [**111, 126**]. The reaction could be considered a first order reaction, so the reaction rate could be defined by equation 3.3.2, where $[TiO_2 : S]$ represents the concentration of semiconductor loaded sites, $[TiO_2]$ the concentration of semiconductor free sites and $[S]$ the concentration of sensitizer molecules in the solution.

$$r = \frac{d[TiO_2 : S]}{dt} = k[TiO_2][S] \tag{3.3.2}$$

Change in dye solution concentration could be considered unvaried. In fact the high concentration (0.5 mM) supplies a number of molecules higher respect the number could be adsorbed by the film. We can define the new kinetic constant k' (equation 3.3.3) and redefine the adsorption rate as a function only of the fraction of TiO_2

coated sites at a certain time t, defined as the coverage θ (equation 3.3.4). The coverage is equal to 1 for a complete coating ($t = \infty$) and equal to 0 for a bare semiconductor substrate ($t = 0$).

(3.3.3) $$k' = k[S]$$

(3.3.4) $$\theta = [TiO_2 : S]_t / [TiO_2 : S]_\infty$$

(3.3.5) $$r = -\frac{d[TiO_2]}{dt} = -\frac{d([TiO_2 : S]_{t=\infty} - [TiO_2 : S]_t)}{dt}$$

(3.3.6) $$r = k'([TiO_2 : S]_{t=\infty} - [TiO_2 : S]_t)$$

(3.3.7) $$-\frac{d(1-\theta)}{dt} = k'(1-\theta)$$

(3.3.8) $$\theta = 1 - e^{-k't}$$

From the equation 3.3.2 is then possible to extract an expression of θ as a function of time and k'.

The study of kinetic process was made using two different methods:

(1) To estimate the integrated area of the adsorption spectra in the wavelengths range 460 nm÷ 800 nm, that represents the main characteristic N719 adsorption range.

(2) To estimate the area of the peak at 540 nm, by e deconvolution of the spectra. Deconvolution was made using e three peaks model, according with previously observations.

Even if the two analysis techniques are quite different, results are equivalent. It is explained by the fact (already observed) that the shape of optical response doesn't change with the increase of dipping time. To analyze the data it was assumed that the saturation value corresponds to a full coverage of semiconductor film. The curves show an high slope for short dipping time and then a slower change in coverage. This behavior is consistent with the theoretical model

previously explained. Figure 3.3.9 reports data obtained from coated films measurements.

The region with higher slope is included between 0 seconds to about 3 hours. Then the saturation is reached at about 16 hours. Anyway it is possible to observe how from 7 hours to 16 hours the variation in coverage is very small. From 3 hours to 7 hours there is a slight variance in data from an exponential behavior. This could be explained by the fact that in this region variation in coverage is very small, so noise (in this case small differences in films structure) could affect the measurements.

The trade of the coverage as a function of time was studied also for dye desorbing solutions. The same techniques were used. Figure 3.3.10 shows the graphs referred to these data. The plot obtained using the area of the decoconvoluted peak at 512 nm is reported.

The data show an irregular behavior is related to which obtained from TiO_2 coated films. In particular even if the first region shows a good agreement, at three hours dipping time the value of coverage obtained with the second method is about 20% lower respect one obtained with the first technique. Then the value at 24 hours dipping time shows a great difference respect the 16 hours dipping time one. This behavior is very different from the previous one.

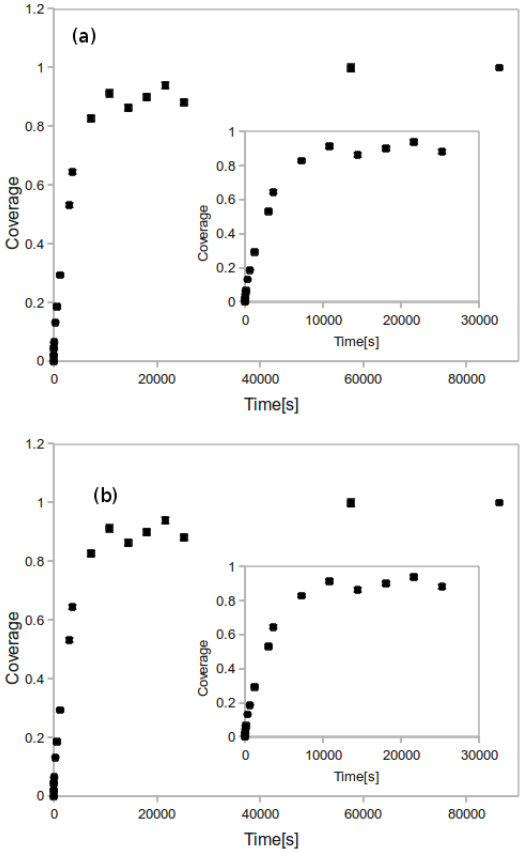

FIGURE 3.3.9. Coverage TiO_2 films versus dipping time in dye solutions. (a) Graph obtained using the integrated area of adsorption spectra in the wavelengths range 460-800 nm. (b) Graph obtained using the area of the peak at 540 nm, obtained by deconvolution technique.

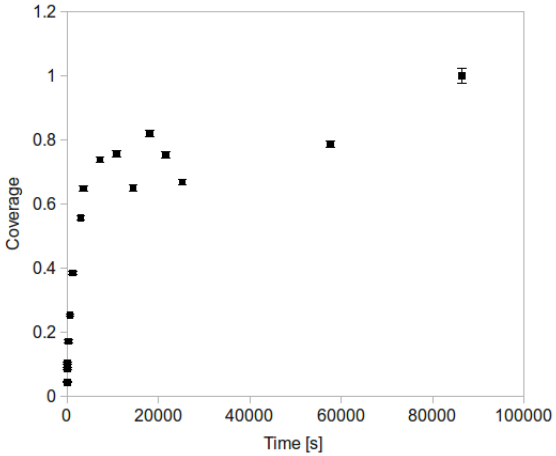

FIGURE 3.3.10. Coverage TiO_2 films versus dipping time in dye solutions. These data were calculated using dye-desorbing solutions.

These discrepancies could be explained supposing that the desorbing technique is not a perfect reaction. It is possible that the process is incomplete and that it is a destructive method, that modify the sensitizer structure.

From this observation it is possible to gather that the spectroscopic analysis of TiO_2 coated films is a more reliable technique, as well as a direct preservative method.

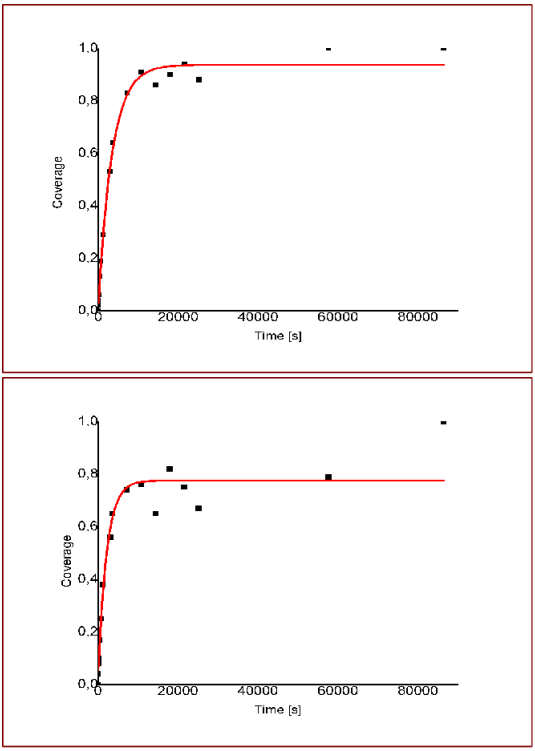

FIGURE 3.3.11. Fits of coverage data, made using the relation $\theta = 1 - e^{-k't}$. On the top The data of the TiO_2 films, on the bottom the data of the dye desorbing solutions.

At least the coverage data were fitted using expression 3.3.4 to obtain the adsorption kinetic constant k'_f (dye-coated films) and k'_s (dye-desorbing solutions). Fit results are showed in figure 3.3.11.

The value of k' obtained are k'_f=(2.89±0.23)10^{-4} s^{-1} and k'_s= (4.65±0.10) $10^{-4}s^{-1}$. Difference between two value points out the importance to have a precise and reliable protocol to study dye loading kinetics.

We can conclude that the adsorption reaction can be treated as following a simple pseudo-first order kinetics, described by the relationship (3.3.8) in terms of saturation ratio and effective rate constant k'_f. This is in contrast with recent kinetic studies where the absorption of N719 on TiO_2 was proposed to be a two-step process, a first rapid growth followed by slow absorption, each characterized by a different kinetics (for N719 the two rate constants are very close). Indeed, the first step was modeled by a pseudo-first order kinetic process and the obtained constant (k'_f = 3 x 10^{-4} s^{-1}) is in excellent agreement with our findings. In a second kinetic study, where adsorption kinetics were followed only up to the first 4 h of dipping time, a pseudo-first order model was similarly proposed, although in that case the kinetic constant (k'_f = 1.6 x 10^{-3} s^{-1}) obtained was slightly different from our and Concina's values [**126, 111**].

Using desorbed data it also possible to calculate the amount of dye adsorbed for different dipping time. Do do this solutions of N719 in NaOH solution were prepared with different concentrations.

Optical density was measured to establish a relationship between dye concentration and adsorbance value. The integrated area of low energy peak was used. The result is the following relationship:

$$A = pC \tag{3.3.9}$$

where A is the peak area, C the dye concentration and p is a constant, calculated as $p = (1.28614 \pm 0.01740) \cdot 10^6$.
Using p it is possible to find concentration of dye in desorbed solution, and then the number of moles adsorbed for each samples. Table 1 shows results obtained.

3.4. Conclusion

We have presented here a new spectroscopic quantitative protocol for real-time investigation of the dye-sensitizer uptaking into TiO_2 semiconductor film for application in DSSCs. The UV-Vis spectra of the dye-coated film have been measured and analyzed as a function of the dipping time of the FTO/TiO_2 substrate into the dye solution, from few s to 24 h. In particular, we show for the first time that the absorption band shapes are not constant over the different dipping time, with a red shift of the main peaks being

TABLE 1. Amount of desorbed time for different dipping time

Time [s]	Amount of desorbed dye [mol/cm^2]	Error [mol/cm^2]
5	0.374582E-9	0.2451739E-10
30	4.680739E-9	1.646607E-10
60	5.616699E-9	2.143609E-10
300	9.350400E-9	2.569695E-10
600	1.387941E-8	3.191857E-10
1200	2.095250E-8	4.612622E-10
3000	3.093853E-8	5.788255E-10
3600	3.606138E-8	6.773828E-10
7200	4.102651E-8	7.206305E-10
10800	4.207353E-8	7.981563E-10
14400	3.613277E-8	6.953878E-10
18000	4.558208E-8	8.550132E-10
21600	4.188194E-8	7.650049E-10
25200	3.714878E-8	7.029011E-10
57600	4.374559E-8	7.913189E-10
86400	5.550572E-8	1.437783E-9

present for dipping times longer than 10 minutes. This behavior was ascribed to aggregation phenomena or protonation equilibrium with the semiconductor oxide. Because of these findings, a new method for determining the relative absorption intensity of the dye-coated films has been proposed, based either on the integration of the whole absorption area in the Vis range or on the integration of the most significant low-energy MLCT peak centered at ca. 540 nm. Both

approaches led to the same conclusions identifying two main temporal regions, one at shorter dipping times (up to 1 h) characterized by a steep increase of the dye loading, and one at longer dipping times, up to 24 h, where the increment of the dye-uptaking is much more modest. The spectroscopic findings have been translated to amounts of adsorbed dye vs dipping time through desorption quantitative studies and kinetics of the adsorption process investigated. For the first time, and in partial agreement with previous kinetic studies, we have found that the whole adsorption process, from few s to 24 h, is very nicely described by a simple pseudo-first order kinetic model, with an observed rate constant of ca. 3 x 10-4 s-1. The combined studies have evidenced that the first minutes (1 h dipping time) are strategic for an effective uptaking of the dye by the TiO2 nanoparticle, with a saturation level reached within the first 6 h. This result is in contrast with the commonly used procedure for dye-uptaking of Ru(II) DSC sensitizers, which implies typical dipping times of 16 to 24 h. We have demonstrated that not only are longer dipping time almost useless for increasing the dye loading into the semiconductor film, but that a change in the dye electronic structure takes place upon increasing the contact time, which could

affect then the photovoltaic response of the photoanode. These results could be exploited for optimizing DSSCs industrial fabrication protocols, where shorter dipping times, or even continuous flow conditions, at no expense of the device efficiency, are crucial for setting up low-cost fast automated procedures.

CHAPTER 4

New counter electrode of DSSC

4.1. Introduction

As explained in previous sections, standard counter electrode used in DSSCs is platinized TCO glass. Platinum has showed to be a good catalytic material for the reduction of tri-iodide (eq. 1.2.10) [**127**]. Anyway platinum is an expensive material (about 50 $ for 1 g) and is not much abundant on earth's crust (5 p.p.b.). Then it is subject to corrosion by liquid ionic electrolyte [**128**]. For this reason the possibility to substitute this material with cheaper and more available material is an outstanding topic in DSSCs development and industrialization path [**129**].

4.2. Carbon Nano-Walls

Carbonaceous materials are attractive to replace platinum due to their high electronic conductivity, corrosion resistance towards iodine, high reactivity for triiodide reaction and low cost [**130, 131**].

Moreover, nano-structuring in general improves the catalytic properties of materials. Several works have been recently published on carbon and carbon nanotubes replacing platinum at the counter-electrode [**132, 133, 134, 135**], while the use of 2-D Carbon nanostructures, (Carbon Nanowalls, CNWs), based on graphene layers, have not yet been explored. In order to test if CNWs are possible candidates for fabricating innovative counter-electrodes for DSSC assembly CNWs have been synthesized by PE-HFCVD (Plasma Enhanced Hot Filament Chemical Vapor Deposition) on different substrates, and their electrical proprieties were studied [**136, 137**]. This study was made at research center ENEA, in Rome.

4.2.1. Experimental section. The PE-HFCVD system (figure 4.2.1) consists of a water cooled stainless steel chamber with a base pressure of 5×10^{-7} mbar. The gas flow, CH_4/He gas mixture, was regulated by mass flow controllers. The vertical filaments were supported from the top while at the bottom they were fixed to a Molybdenum (Mo) plate which was left suspended and acted as a common ground for the heating DC current. The substrate heating assembly was made as follow: a water cooled copper plate acted both as thermal reference and as mechanical support while a second stainless steel plate was mechanically supported onto the

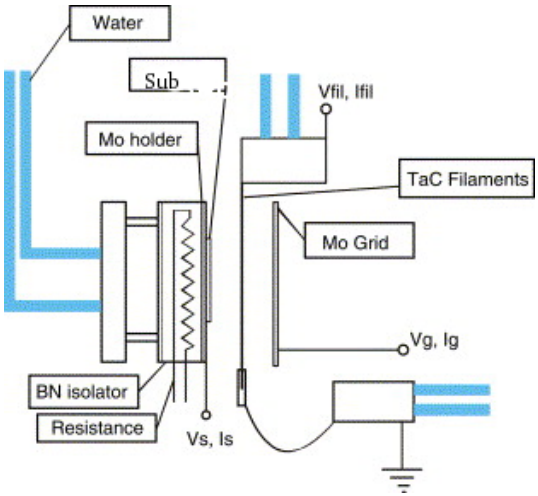

FIGURE 4.2.1. PE-HFCVD system. Here V_{fil} and I_{fil} are the filament voltage and current, V_m is the grid bias voltage and V_s is the substrate bias voltage.

copper plate with thermal breaks. A Boron Nitride (BN) plate electrically isolated the Mo substrate holder from the steel plate. The substrate heating element was buried inside the BN together with a reference (Type K) thermocouple and could heat and maintain the apparatus at the desired temperature by means of a regulated AC power supply.

A substrate temperature of 700 °C and a filament temperature above 2100 °C was utilized. A plasma (30 V, 1 A) was generated by

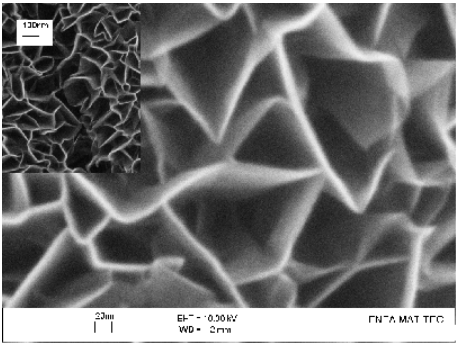

FIGURE 4.2.2. SEM image of CNWs film.

biasing the grid. For this work CNWs films were deposited onto quartz and Titanium substrates. Furthermore, films of different thickness were synthesized in order to vary the sheet resistance of the samples.

Films morphology was investigated by Scanning Electron Microscope (SEM) and Transmission Electron Microscopy (TEM). SEM images (figure 4.2.2) show layers of graphene assembled onto a substrate in a sort of random honeycomb structure on the whole substrate. This structure allows to provide a great effective area for tri-iodide reduction.

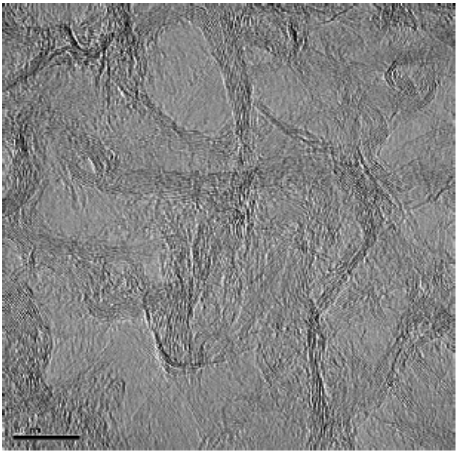

FIGURE 4.2.3. TEM image on a scraped sample.

TEM images (figure 4.2.3) on a scraped sample show that the material is composed of few to several graphene layers. This structure allows to realize samples of different thickness, increasing the numbers of graphene layers.

Raman spectrum (figure 4.2.4) shows the characteristic peaks of CNWs: G-band of the graphite and D-band due to the imperfection of the graphitic order.[**138, 139**]

The CNWs film thickness can be varied by changing the deposition time. Resistance measurements in DC current allows to calculate the sheet resistance of the films, as a function of the thickness of

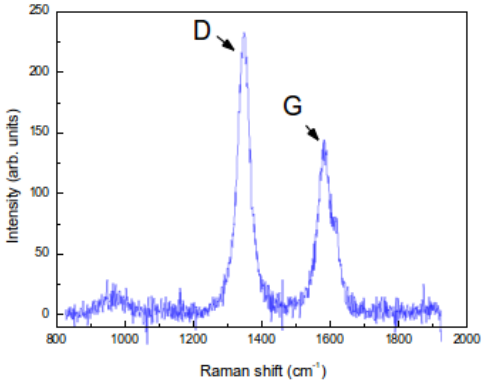

FIGURE 4.2.4. Raman spectrum of a CNWs sample.

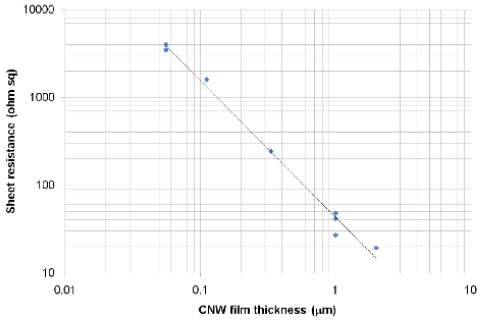

FIGURE 4.2.5. CNWs films resistance as a function of film thickness.

the film. Results obtained (figure 4.2.5) show as the film resistance decreases increasing the thickness, with a linear relationship.

Photovoltaic devices were realized using FTO glasses Solaronix, 10 $\Omega/\square$ as substrates. Active area has a rectangular shape 0.5 x 1.0 cm. As TiO_2 was used a mixture of HT Solaronix, with particle size about 20 nm, and R Solaronix, with particle size about 400 nm, with a weight ratio of (7:3). As sensitizer was used N719 (Solaronix), in ethanol solution 0.5 mM. The electrolyte was composed by I_2 0.05 M, LiI 0.5 M , 4-tert-butylpyridine 0.5 M in acetonitrile. Devices was sealed using Surlyn 60 μm thick.
Cells characterization was made using an Oriel Xe lamp 100 mW/cm^2 with a UV cut filter and data was collecting by a PARSTAT 2273 Potenziostat/Galvanostat.

4.2.2. Results. Results is showed in table 1. It is important to observe how the counter electrode affects both the current density and the open circuit voltage. The standard device (Pt as CE) has an efficiency about 3.5%. This not an high results, if compared with results in literature. Anyway the aim of this work was not to obtain an optimized device, but just a comparative study on different materials.

The thickness of CNWs film on quartz has a strong consequence on photocurrent, probably not only for the difference in sheet resistance, but also for increasing in catalytic effect. As results, using 2

TABLE 1. Results obtained using different counter electrodes.

Sample	Thickness [μm]	V_{OC}[mV]	J_{sc}[mA/cm^2]	Eff. %	FF
FTO+Pt	-	686	14.0	3.5	0.40
Quartz+CNWs	1	595	6.4	0.9	0.24
Quartz+CNWs	2	765	12.0	1.9	0.21
Ti+CNWs	2	825	12.2	3.5	0.35

μm thick CNWs film instead of 1 μm, we obtained a double short circuit current density (12 mA/cm^2), very similar to one obtained with a standard device (14 mA/cm^2). Anyway best results was obtained using Ti as substrate. It is caused not only for a good current density, but also cause to the high open circuit voltage and fill factor.

The open circuit voltage is very dependent from counter electrode type. In particular it is very low using 1 μm thickness CNWs film, and increases increasing thickness, exceeding the value of a standard device. This behavior is explainable with the fact that open circuit potential depends on the electrochemical potential of electrons, that is related to the concentrations of the oxidized and reduced species of the redox system, and so to the catalytic efficiency of counter electrode.

It is possible to understand the low fill factor obtained using quartz as substrates from the I/V characteristic curves (figure 4.2.6). The

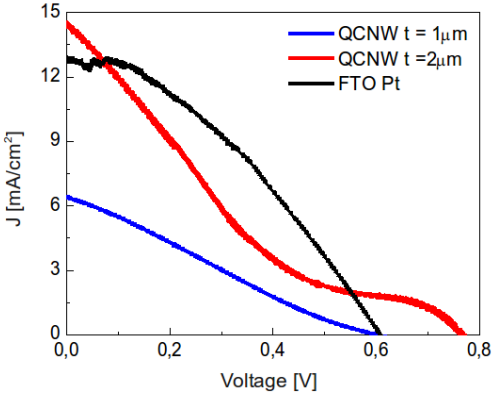

FIGURE 4.2.6. I/V characteristic curves for systems with CNWs on quartz as counter electrodes in comparison with one with standard (Pt) counter electrode.

shape of the curves shows a high series resistance. Then for the thicker CNWs film the presence of capacitive effects. This behavior is not present in devices with Ti as substrate (figure 4.2.7).

Results obtained shows as carbon nano-walls appear to be a promising substitute for platinum. The limit of this technique is the choice of substrate, that has to be resistant to high temperature and to electrolyte solution.

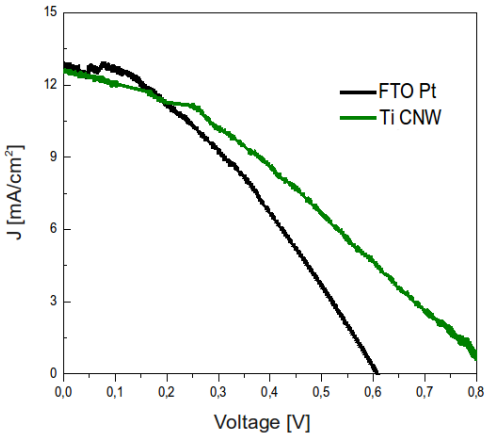

FIGURE 4.2.7. I/V characteristic curves for devices with CNWs on Ti and Pt on FTO as counter electrodes.

4.3. PEDOT

Other than carbon materials to replace platinized counter electrodes, poly(3,4-ethylenedioxythiophene) (PEDOT) could be an interesting choice. The interesting for this material is caused by its high conductivity, low band gap (1.6 eV), electrochemical reversibility, transparency, stability, and high catalytic activity compared to other polythiophenes. Then electro-deposited PEDOT on TCO substrate has already showed good performances in DSSCs, reaching

efficiency of almost 8%. [**140**]

Electro-polymerized PEDOT films have showed to have a high conductivity, even if it is about four order of magnitude higher respect a FTO- coated glass. Then it exhibits homogeneous morphologies with high porosity. The porosity enables to have a high specific surface area and as consequence an high catalytic efficiency. The use of porous material allows then the post fictionalization of the pore walls with the suitable dopant, to increase conductivity.

In this section will be presented results of use of PEDOT counter electrodes prepared by electrochemical polymerization on plastic flexible substrate. The study was performed at LPI-EPFL, Lausanne.

4.3.1. Experimental section. PEDOT films were prepared by electrochemical polymerization using EDOT monomer ([**141, 142**]).

The polymer was deposited potentiostatically at a DC potential of +1.2 V using Eco Chemie AUTOLAB 1260 in a three-electrode system comprised of PEDOT coated sheet, as a working electrode, platinum rod as the counter electrode, and Ag/AgCl at 25° C as the reference electrode. The working electrode was placed parallel to the working electrode in a solution containing the ionic liquids

and 0.1 M monomer. The potential was applied for a period of 300 seconds, to coat the PEDOT flexible sheets with polymer layers and to use them as ITO and metal free electro catalyst. After the polymerization process the film was removed from growth solution, washed repeatedly with isopropyl alcohol to get rid of any unreacted monomer as well as ionic liquids and finally heated at 60° C for 30 minutes. Further to increase the conductivity the obtained film was dipped in ethylene glycol for 30 minutes and fired at 80° C for 15 minutes.

DSSCs were prepared using standard working electrodes, with different thickness, to optimized results. Dyes used are showed in figure 4.3.1. D21L6 is a metal free organic dye, that showed an efficiency about 6% in solar cells with ionic liquid based electrolyte [**143**]. Y123 is an other organic dye that shows an efficiency almost about 9% with a Co(II)/Co(III) based electrolyte [**144**].

Four different electrolyte were been used: Z960 (1 M DMII, 0.05 M LiI, 0.03 M I_2, 0.1 M GuNCS, 0.5 M TBP), JH34 (0.6 M DMII, 0.05 M LiI, 0.03 M I2, 0.05 M GuNCS, 0.25 M TBP), JH70 (0.22 M Co^{2+}, 0.05 M Co^{3+}, 0.1 M $LiClO_4$, and 0.2 M TBP, with a Cobalt tridentate redox couple) and JH180, with a Cobalt tris-Bipyridine redox couple.

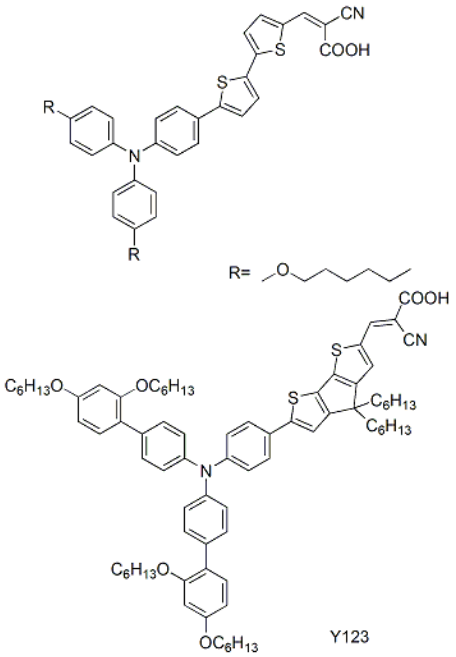

FIGURE 4.3.1. Dyes used for this study: on the top D21L6, on the bottom Y123.

4.3.2. Results. First devices were made using as working electrode a transparent TiO_2 film, with a thickness of 5.8 μm, stained with a 0.3 mM solution of D21L6 in ethanol, and Z960 electrolyte. The same working electrodes electrodes were tested with a PEDOT and a standard (Pt on FTO) counter electrodes (respectively device **1** and **2**).

Table 2 shows the results obtained. The big difference in efficiency is due to the high series resistance of PEDOT film on a plastic (insulator) substrate, that reduces current density and fill factor, especially at high intensity of illumination (figure 4.3.2).

TABLE 2. Comparison between two DSCs with the same working electrode and different counter-electrode, at 1 Sun illumination.

	FTO+Pt	PEDOT
Eff. %	5.75	0.73
J_{SC} [mA/cm^2]	11.32	3.98
V_{OC}[mV]	732.67	719.87
FF	0.69	0.23

Also the analysis of current dynamics (figure 4.3.3) shows as increasing the current density has not a linear behavior with illumination power. This could mean that the counter electrode has not enough catalytic efficiency.

For this reason the first step was to optimize PEDOT film thickness, and as consequences the effective area. In fact increasing polymerization time, it is possible to increase the thickness of the film. It is important to point out as there is a limit in thickness due to the adhesion of the PEDOT on the substrates. A too thick film has a bad adhesion on plastic substrates that does not allow to realize an efficient solar cell device.

Anyway doubling deposition time it possible to obtain a good film, both for the catalytic proprieties and for structural proprieties. Devices realized (device **3**) with this film as counter electrode showed an increase both in current density and in fill factor. The efficiency

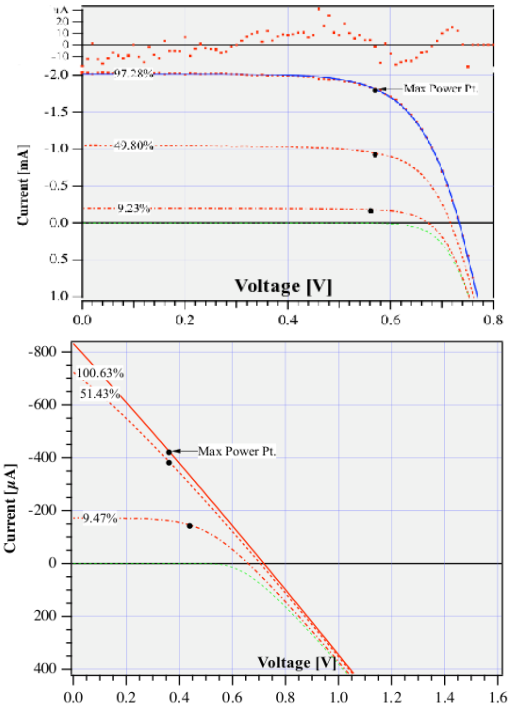

FIGURE 4.3.2. I/V characteristic curve of DSCs with a standard counter electrode (top) and a PEDOT counter electrode (bottom).

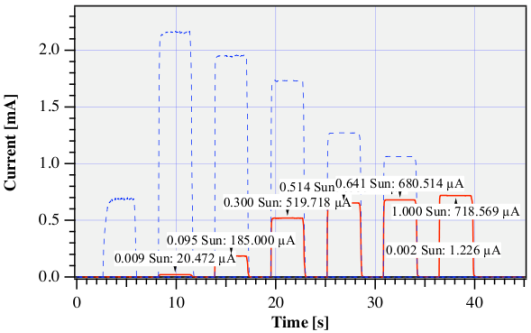

FIGURE 4.3.3. Current density at different illumination for device **1**

reached was 1.65%, with a short circuit current density about 8.04 mA/cm^2, a V_{OC} about 693 mV and a fill factor of 0.30. I/V characteristic curve (figure 4.3.4) shows a decrease in sheet resistance, and also the current dynamics shows a more linearity in current response respect illumination intensity.

Next step consists in use doped PEDOT film. In this way it is possible to increase film conductivity. Then changing dye and electrolytes it is possible to increase open circuit voltage. In particular three electrolyte were tested. JH34 is similar to Z960, but the less amount of TBP contributes to reduce loss in current density. JH70 and JH180 are two cobalt complexes based electrolyte, that could allow an increase in V_{OC}.

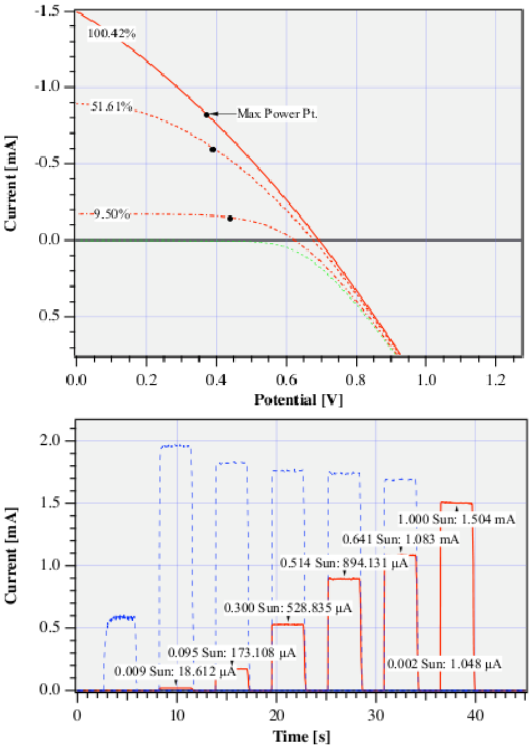

FIGURE 4.3.4. I/V characteristic curve and current dynamics obtained for device **3**. In this way it is possible to reach 1.65% of efficiency.

Table 3 shows results obtained.

Devices **5** and **6** show an increase in open circuit voltage respect devices **4**, as expected. Then there is a low increase in current density, especially for devices **6** and in fill factor. These elements

TABLE 3. Results obtained for devices **4**, **5** and **6**.

	JH34 (**4**)	JH70 (**5**)	JH180 (**6**)
Eff. %	2.38	3.96	4.22
J_{sc} [mA/cm^2]	10.18	10.75	10.91
V_{OC}[mV]	680.14	942.39	829.52
FF	0.34	0.39	0.47

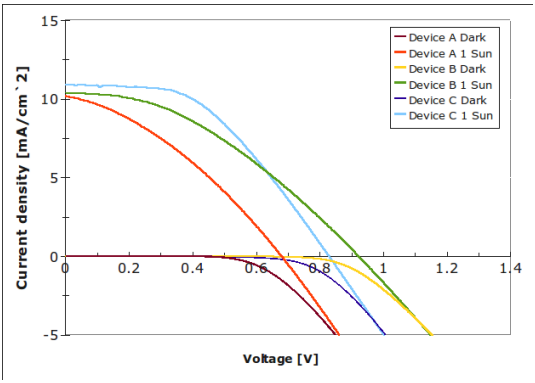

FIGURE 4.3.5. I/V characteristic curves for device **5** and **6** at different illumination.

allow to reach an efficiency of 3.96 for device **5** and of 4.22% for device **6**. I/V curve for devices **5** and **6** are showed in figure 4.3.5. Different illumination curves are reported it is interesting to note how for low illumination intensity the shape of curves are similar for both devices, while for full illumination (1 Sun) the shape start to change.

4.4. Conclusion

Two different materials to replace platinum in counter-electrodes are tested. Carbon nano-walls belongs to a class of versatile and economic materials. Results obtained in this work are very encouraging. In fact open circuit voltage and current density are suitable with standard devices in the same condition. The low fill factor is due mainly to the substrate used, and increases using Ti in place of quartz.

The study on PEDOT counter-electrode has the peculiarity to use a flexible plastic substrate. This fact, combined with the transparency of PEDOT, allows to think about original application of DSSC (such as building integration), and also to realize a low-cost device. Efficiency reached exceeds 4%. Also in this case the low fill factor is penalizing for photovoltaic performances.

CHAPTER 5

Electrochemical Impedance Spectroscopy using a three electrodes devices

5.1. Introduction

Electrochemical impedance spectroscopy (EIS) is a useful tool to study DSSCs. This technique permits to study the kinetics of many process with different response time, using a wide frequencies range [**145, 146, 147**]. Until now a lot of study are made using conventional DSSCs in a two-electrode electrochemical configuration. Typically result obtained is a three semicircles shape Nyquist diagram [**23**]. In many cases the process at higher frequencies (1kHz-10kHz) is related to charge transfer process at platinum/electrolyte interface, medium frequencies phenomena (10-100Hz) is related to semiconductor/electrolyte interface processes (diffusion in TiO_2 and back reaction with trioxide species), and then the lower frequencies semicircle (0.001-0.1 Hz) to charges diffusion into electrolyte

[**148, 149**]. A lot of information could be drawn from impedance data, for example the electrons lifetime in semiconductor film, the internal cell resistances, properties of hole transport materials, electron diffusion length in semiconductor and the density of electronic states [**150, 127, 151, 152, 153, 154**].

However the complexity of the system and the high number of processes involved make data interpretation difficult and ambiguous. In particular the low frequencies semicircles could overlap with middle frequencies one, making hard distinguish the single contributions [**155, 156**]. Moreover in a 2-electrode DSSC the cell voltage is referred to the cathode potential, that is not defined under bias illumination. *T. Hoshikawa et al* proposed to use three electrode system in EIS measurements, to distinguish easily different contributions, but affirm the difficult to insert e reference electrode in a DSSC standard device, because its thickness [**157**]. So they use a glass vessel three electrode cell instead a typical sandwich-type device. This device is structurally different from a standard DSSC, and could present some differences in electronic processes.

In this chapter I will explain how we manage to realize a three electrode device very close to a standard device, and i will present

the first results, those permit to assign a more reliable meaning to EIS experiment.

5.2. Transmission line model

The most used model to represent the equivalent circuit for a DSC is the transmission line model, where the modeled elements are: the contact and the FTO substrates (a ohmic resistance R_{se}), the interface TiO_2|electrolyte, the interface Pt|electrolyte and the electrolyte medium [**158, 45, 23**].

For the FTO part, the impedance is calculated by:

$$Z = (\frac{R_r R_{tr}}{i + i\frac{\omega}{\omega_r}}) coth[(\frac{\omega_r}{\omega_{tr}})^{0.5}(1 + \frac{i\omega}{\omega_r})^{0.5}] \tag{5.2.1}$$

where R_r is the charge recombination with the triodide ions resistance and R_{tr} is the charge transport in semiconductor film resistance, while ω_r ($\omega_r = \frac{1}{\tau_r}$) and ω_{tr} are the corresponding characteristic frequencies.

If the recombination resistance is higher respect R_{tr}, the eq. 5.2.1 represents the Warburg element:

$$Z = (\frac{R_{tr}}{C})^{0.5}(i\omega)^{-0.5} \tag{5.2.2}$$

where C is the total capacitance [**159, 45**]. Instead for lower recombination resistance, the eq. 5.2.1 turns into Gerischer impedance:

$$Z = (\frac{R_{tr}R_r}{1+\frac{i\omega}{\omega_r}})^{0.5} \tag{5.2.3}$$

For the counter electrode interface, impedance is expressed like:

$$Z = (\frac{iR_{ct}}{i - R_{ct}C_{dl}\omega})^{0.5} \tag{5.2.4}$$

where R_{ct} is the charge transfer resistance at the interface and C_{dl} is the double layer capacitance.

The diffusion of I_3^- within a thin layer cell is usually described by a Nernst diffusion impedance Z_N, that could expressed how:

$$Z_N = \frac{Z_0}{(i\omega)^\alpha} tanh(i\tau_d\omega)^\alpha \tag{5.2.5}$$

where ω is the angular frequency and R equals 0.5 for a finite length Warburg impedance. Z_0 and τ_d are the Warburg parameter and characteristic diffusion time constant.

5.3. Experimental details

The major difficulty in realizing a three electrodes device is to insert the reference electrode without any contact with electrodes.

In fact in a standard configuration the two electrodes are separated using a thin polymeric sealant of few tens of micron.

To ride out this problem we have used a 25 μm thick platinum foil as reference electrode and we have removed part of the conductive film of (SnO_2:F) from glass substrates, to create an insulating area were positioning the reference electrode.

Two frames of Surlyn® 2 cm x 1.5 cm and 2 mm width were cut and the system was close on an hot plate at 125 °C using a press. Reference electrode is placed between the two Surlyn® frame, to permit a good sealing of the device, and in correspondence of the etching glasses to avoid any electric contact between reference electrode and DSC electrodes (figure 5.3.1). After the sealing a ionic electrolyte was put into the device through the hole in cathode by vacuum back filling. The electrolyte was a valeronitrile/ acetonitrile solution (15:85) with 0.6 M BMII, 0.03 M I_2, 0.1 M guanidinium thyocyanate and 0.5 M 4-tert-butylpyridine. Then the hole is closed using Surlyn®.

Photocurrent - voltage characteristic measurement was made using a Oriel Solar Simulator 81150 equipped with a Xenon lamp and a filter 1.5 AM direct. Measurements under illumination were made under 450 mW/cm^2 light power (1 Sun). EIS measurements were

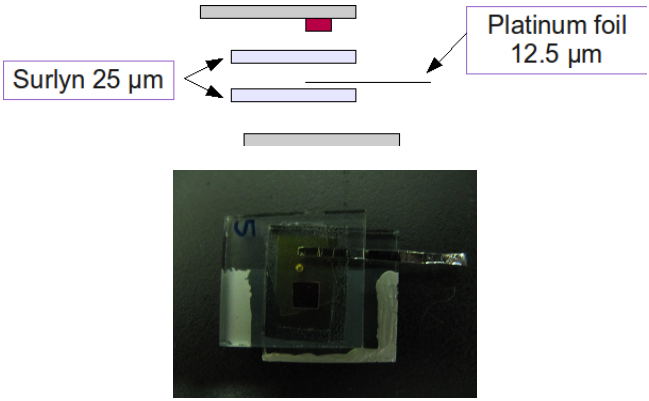

FIGURE 5.3.1. Three electrode solar cell device. It is visible the reference electrode inside the cell.

performed using Parstat 2263 potenziostat. Spectra were recorded at open circuit voltage under illumination of 1 Sun and in dark condition at different bias. The frequency was spanned between 10 mHz and 10 kHz and the amplitude of the alternative voltage signal was 15 mV. For two-electrode measurements the reference contact was positioned at photo-cathode.

5.4. Results

Realized device shows an efficiency of 6.30%, a V_{oc} of 708 mV, a short circuit current density about 13.02 and a fill factor of 0.68.

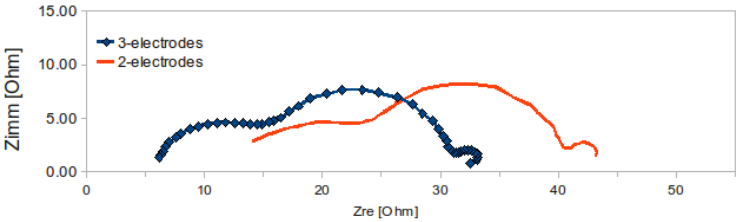

FIGURE 5.4.1. Nyquist plot for 2-electrodes and 3-electrodes system. Measurements was performed under 1 Sun illumination.

In figure 5.4.1 are showed the Nyquist plot obtained for 2-electrodes and 3-electrodes setup measurements under 1 Sun illumination.

The most evident difference for this plot is the shift of the graph on the x-axis. This shift corresponds to an increase in ohmic resistance. The resistance of device in 3-electrodes system correspond to FTO substrate resistance plus electrolyte ohmic resistance. In 2-electrodes system the total resistance includes an other FTO resistance, related to reference electrode on counter electrode. Except this the shape of the two graphs appears the same. Anyway more differences come out observing the Bode graph (figure 5.4.2). In this case, even if the peak frequencies stay almost the same, there is a difference in peaks shape.

These differences pointed out how the impedance spectra for an efficient counter electrode is related mainly to TiO_2|electrolyte

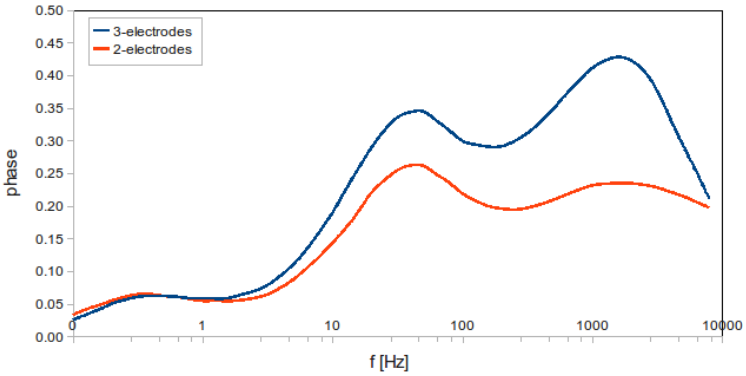

FIGURE 5.4.2. Bode diagram for 2-electrodes and 3-electrodes system under 1 Sun illumination.

interface. Then it is clear how the 3-electrodes setup could be an useful tool when the aim is obtain quantitative information by EIS measurements.

Measurements under dark at different bias were performed for 3-electrodes setup, and are showed in figure 5.4.3. As it is expected there is an increase in charge recombination resistance when the applied bias is reduced respect open circuit voltage value. Data obtained were fitted using the equivalent circuit showed in figure 5.4.4. This model is similar to standard transmission line model, but some changes were made [**160**]. With the new setup proposed the interface Pt| electrolyte is not considered, because the reference electrode

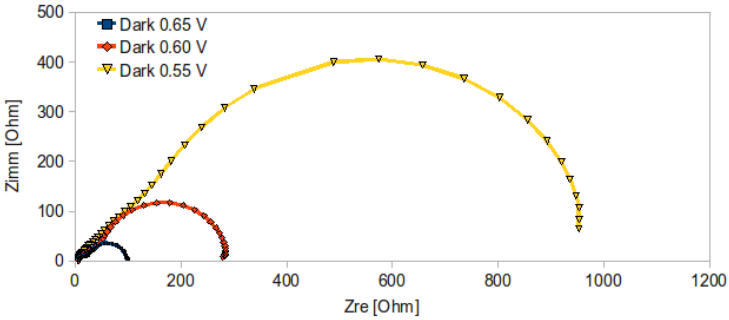

FIGURE 5.4.3. Nyquist plot obtained under dark condition, for different applied bias. Bias near to open circuit voltage are considered.

does not involve this element of the cell.

In particular, it has been considered that the electrons can be accumulate into the TiO_2 film with a certain time constant τ_p, and for longer times (lower frequency), the electrons can move through the total resistance R_p. The resistance of electrolyte inside TiO_2 pores ρ_s could be neglected. The reaction at the surface of the working electrode has been considered as a simple charge transfer in solution, and therefore the interface has been modeled as a pure double layer C_{dl} in parallel with the charge transfer resistance R_{ct}. An extra element, $Z_s = Z/A_s$, has been considered for the fitting of the spectra, which takes into account the ratio between the impedance

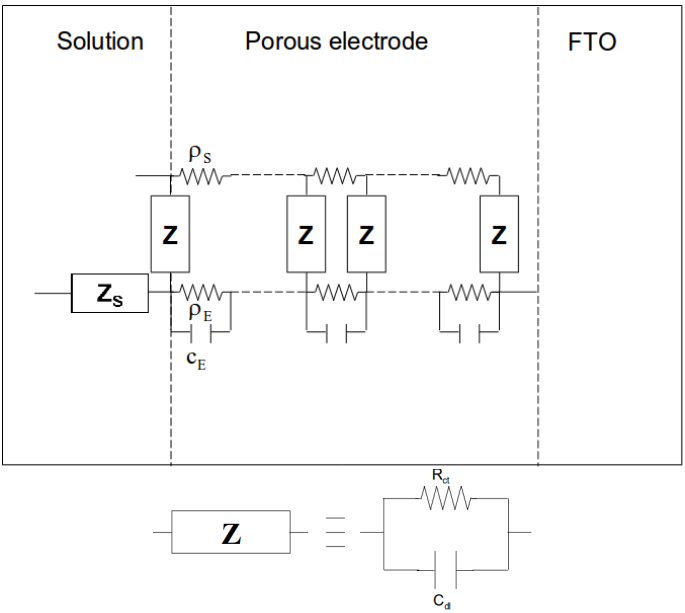

FIGURE 5.4.4. Equivalent circuit used to fit impedance data under illumination. ρ_s is the electrolyte resistance inside TiO_2 porous structure, ρ_E and C_E are the resistance and the capacitance in the TiO_2 pores, Z represents the interface TiO_2|electrolyte, Z_s relates impedance inside semiconductor film and impedance of the external layer.

in the pores and the impedance of the external layer of TiO_2 directly exposed to the bulk of the electrolyte solution. The interface FTO|TiO_2 is not considered, in fact it involve too high frequencies. This circuit is represented by the following expression:

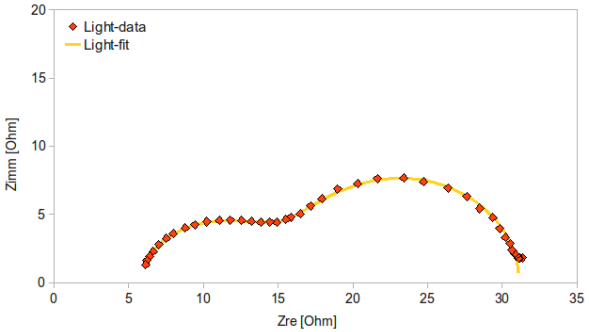

FIGURE 5.4.5. Experimental data and fit results for measurements under 1 Sun illumination.

$$Z = \frac{R_p}{(1 + i\omega\tau_p)} \frac{1}{B} \left\{ \frac{1 + A_s B \tanh(B)}{\tanh(B) + A_s B} \right\} \tag{5.4.1}$$

where $\tau_p = R_p C_p$ and n is a ideality factor related to C_p and $B = \sqrt{\left[\frac{R_p}{Z(1+i\omega\tau_p)}\right]^n}$.

This model fits good the experimental data, as showed if figure 5.4.5-5.4.8. Table 1 shows the parameters obtained fitting some measured data. Measurements under illumination and under dark at different bias (0.65 V, 0.60 V and 0.55 V) are fitted.

R_{se} represents the series resistance of the system and it is almost the same for all measurements. Instead other parameters show to be more bias-dependent. As previously discussed R_{ct} increases with

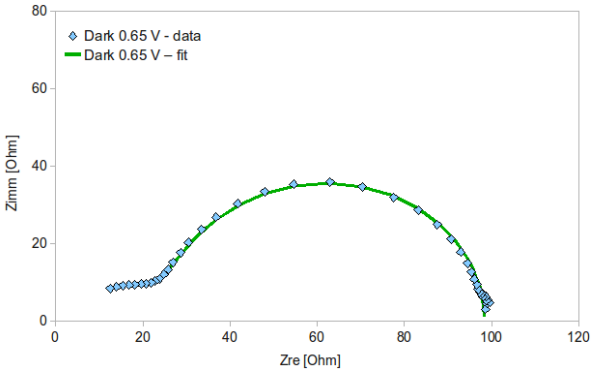

FIGURE 5.4.6. Experimental data and fit results for measurements in dark with 0.65 V bias.

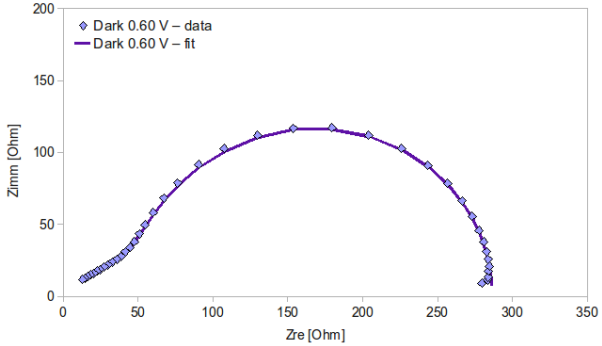

FIGURE 5.4.7. Experimental data and fit results for measurements in dark with 0.60 V bias.

lower bias, when recombination becomes less important. Electron lifetime in pores τ_p is strongly dependent on imposed bias. It is lower

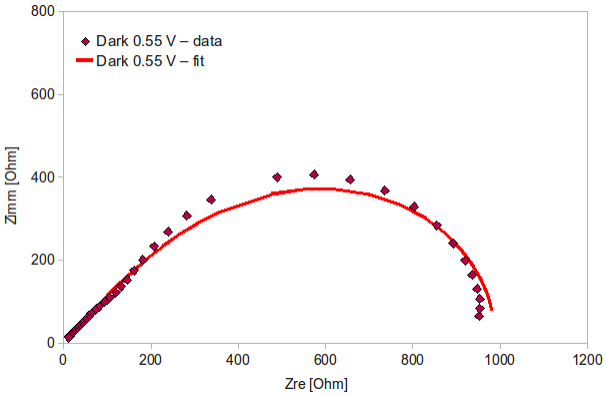

FIGURE 5.4.8. Experimental data and fit results for measurements in dark with 0.55 V bias.

TABLE 1. Fit results for light and dark measurements.

	Light	Dark 0.65 V	Dark 0.60 V	Dark 0.55 V
$R_{se}[\Omega cm^2]$	5.88	5.55	5.54	5.54
$C_{dl}[Fcm^{-2}]10^{-6}$	49.4	42.5	118.0	0.42
$R_{ct}[\Omega cm^2]10^2$	1.64	5.32	4.28	5380
$R_p[\Omega cm^2]$	11.2	22.3	81.3	0.72
$\tau_p[s]10^{-4}$	0.747	0.955	1.14	1.32
A_s	4.76	3.47	0.45	0.55
n	0.889	0.925	0.941	0.753

under illumination at open circuit condition, when there is a strong recombination with electrolyte species, and increase when the bias decreases and recombination becomes slower. Also A_s is strongly

dependent from applied potential, because the non homogeneous polarization of TiO_2 film.

5.5. Conclusion

A new setup for EIS measurements on DSSCs was proposed. The device realized has photovoltaic performances near to a standard device and has the same electronic process. The inclusion of a reference electrode allowed to separate the contribution of different device elements and to analyze in detail the porous electrode. Then a new equivalent circuit was proposed to model and analyze impedance data. This model shows a good agreement with experimental data and permit to analyze the charge transport inside the semiconductor medium.

Bibliography

[1] B. and O'Regan and M. Gratzel. *Nature*, 353:737–739, 1991.

[2] M. Gratzel. *Nature*, 414(November), 2001.

[3] a. Yella, H.-W. Lee, H. N. Tsao, C. Yi, a. K. Chandiran, M. K. Nazeeruddin, E. W.-G. Diau, C.-Y. Yeh, S. M. Zakeeruddin, and M. Gratzel. *Science*, 334(6056):629–634, November 2011.

[4] H. Hagfeldt, A.; Boschloo, G.; Sun, L.; Kloo, L.; Pettersson. *Chem. Rev.*, 110:6595–6663, 2010.

[5] C. M. Elliott. *Nature Chemistry*, 3(118), 2011.

[6] Armaroli, N. and Balzani, A. *Angew. Chem., Int. Ed.*, 46(52), 2007.

[7] A. J. Nozik and J. Miller. *Chem. Rev.*, 110:6443, 2010.

[8] M. Planck, M. Masius. *The Theory of Heat Radiation*. 1914.

[9] P. Würfel. *The Physics of Solar Cells*. 2005.

[10] Www.astm.org. ASTM Standard C33; 2003; "Specification for Concrete Aggregates;" ASTM International; West Conshohocken;.

[11] A. E. Becquerel. *C. R. Acad. Sci. Paris*, 9:561, 1839.

[12] W. Siemens. *Eng. Mag.*, 32:392, 1885.

[13] R. S. OHL, 1941.

[14] M Green. *Physica E: Low-dimensional Systems and Nanostructures*, 14(1-2):65–70, April 2002.

[15] A. N M Green, E. Palomares, S. a Haque, J. M Kroon, and J. R Durrant. *The journal of physical chemistry. B*, 109(25):12525–33, June 2005.

[16] J. Mattheis, J. Werner, and U. Rau. *Physical Review B*, 77(8):1–13, February 2008.

[17] M. Grätzel. *Journal of Photochemistry and Photobiology C: Photochemistry Reviews*, 4(2):145–153, October 2003.

[18] D. Cahen, G. Hodes, M. Gra, J. Franc, and I. Riess. *Journal of Physical Chemistry B*, 104:2053–2059, 2000.

[19] P.V.V. Jayaweera, a.G.U. Perera, and K. Tennakone. *Inorganica Chimica Acta*, 361(3):707–711, February 2008.

[20] L. Peter. *Journal of Electroanalytical Chemistry*, 599(2):233–240, January 2007.

[21] B. A Gregg. *Coordination Chemistry Reviews*, 248:1215–1224, 2004.

[22] P. R. Somani, S. P. Somani, M. Umeno, and A. Sato. *Applied Physics Letters*, 89(8):083501, 2006.

[23] L. Bay and K. West. *Solar Energy Materials and Solar Cells*, 87(1-4):613–628, May 2005.

[24] J. Halme, P. Vahermaa, K. Miettunen, and P. Lund. *Advanced materials (Deerfield Beach, Fla.)*, 22(35):E210–34, September 2010.

[25] J. Bisquert. *Physical Chemistry Chemical Physics communication*, 10(1):49–72, January 2008.

[26] M. Penny, T. Farrell, and C. Please. *Solar Energy Materials and Solar Cells*, 92(1):11–23, January 2008.

[27] T. W. Hamann, Rebecca a. Jensen, Alex B. F. Martinson, Hal Van Ryswyk, and Joseph T. Hupp. *Energy & Environmental Science*, 1(1):66, 2008.

[28] J. Cabanillas-Gonzalez, T. Virgili, a. Gambetta, G. Lanzani, T. Anthopoulos, and D. de Leeuw. *Physical Review Letters*, 96(10):6–9, March 2006.

[29] M. Wei, Y. Konishi, H. Zhou, M. Yanagida, H. Sugihara, and H. Arakawa. *Journal of Materials Chemistry*, 16(13):1287, 2006.

[30] S. Y. Kim. *Journal of Applied Physics*, 95(5):2560, 2004.

[31] J. S. Bendall, L. Etgar, S. C. Tan, N. Cai, P. Wang, S. M. Zakeeruddin, M Gratzel, and M. E. Welland. *Energy & Environmental Science*, 4(8):2903, 2011.

[32] J X Wang, C M L Wu, W S Cheung, L B Luo, Z B He, G D Yuan, W J Zhang, C S Lee, and S T Lee. *J. Phys. Chem. C*, 114(31):13157–13161, 2010.

[33] M Smirnov and R Baddour-Hadjean. *The Journal of chemical physics*, 121(5):2348–55, August 2004.

[34] A. Reale, T. M. Brown, A. Di Carlo, F. Giannini, F. Brunetti, E. Leonardi, M. Lucci, M. L. Terranova, S. Orlanducci, E. Tamburri, F. Toschi, and V. Sessa. *Proceedings of SPIE*, 6334:63340Y–63340Y–8, 2006.

[35] Z. Wang, H. Kawauchi, T. Kashima, and Hi. Arakawa. *Coordination Chemistry Reviews*, 248(13-14):1381–1389, July 2004.

[36] D. Kuang, J. Brillet, P. Chen, M. Takata, S. Uchida, H. Miura, K. Sumioka, S. M Zakeeruddin, and M. Grätzel. *ACS nano*, 2(6):1113–6, June 2008.

[37] J. Wu, G. Chen, C. Lu, We. Wu, and J. Chen. *Nanotechnology*, 19(10):105702, March 2008.

[38] H Yanagi. *Applied Surface Science*, 113-114:426–431, April 1997.

[39] N. Papageorgiou, M. Grätzel, and P.P. Infelta. *Solar Energy Materials and Solar Cells*, 44(4):405–438, December 1996.

[40] J. Nelson, S. Haque, D. Klug, and J. Durrant. *Physical Review B*, 63(20):1–9, May 2001.

[41] J. Nelson. *Physical Review B*, 59(23):15374–15380, June 1999.

[42] K. Schwarzburg, R. Ernstorfer, S. Felber, and F. Willig. *Coordination Chemistry Reviews*, 248:1259–1270, 2004.

[43] M Penny. *Journal of Photochemistry and Photobiology A: Chemistry*, 164(1-3):41–46, June 2004.

[44] M. Grätzel. *Inorganic chemistry*, 44(20):6841–51, October 2005.

[45] J. Bisquert. *Physical Chemistry Chemical Physics communication*, 5:5360–5364, 2003.

[46] S Ito, T Murakami, P Comte, P Liska, C Gratzel, M Nazeeruddin, and M Gratzel. *Thin Solid Films*, 516(14):4613–4619, May 2008.

[47] G. Khelashvili, S. Behrens, H. Bo, A. Hinsch, K. Skupien, and E. Dinjus. *Journal of Clouster Science*, 18(1):141–155, 2007.

[48] C Pérez León, L Kador, B Peng, and M Thelakkat. *The journal of physical chemistry. B*, 110(17):8723–30, May 2006.

[49] Md. K. Nazeeruddin, R. Humphry-Baker, P. Liska, and M. Grätzel. *The Journal of Physical Chemistry B*, 107(34):8981–8987, August 2003.

[50] M K Nazeeruddin, A Kay, E Miiller, P Liska, and N Vlachopoulos. (4):6382–6390, 1993.

[51] S. Hwang, J. Lee, C. Park, H. Lee, C. Kim, C. Park, M. Lee, W. Lee, J. Park, K. Kim, N. Park, and C. Kim. *Chemical Communications*, (46):4887, 2007.

[52] Z. Wang and F. Liu. *Frontiers of Chemistry in China*, 5(2):150–161, May 2010.

[53] Klaus Schwarzburg and Frank Willig. *The Journal of Physical Chemistry B*, 103(28):5743–5746, July 1999.

[54] T. Stergiopoulos, E. Rozi, C. Karagianni, and P. Falaras. *Nanoscale research letters*, 6(1):307, January 2011.

[55] M. Durr, a. Yasuda, and G. Nelles. *Applied Physics Letters*, 89(6):061110, 2006.

[56] X. Liu, W. Zhang, S. Uchida, L. Cai, B. Liu, and S. Ramakrishna. *Advanced materials (Deerfield Beach, Fla.)*, 22(20):E150–5, May 2010.

[57] Y Tak. *Thin Solid Films*, 411(1):12–16, May 2002.

[58] P. Vacca, M. Petrosino, a. Guerra, R. Chierchia, C. Minarini, D.D. Sala, and a. Rubino. *Journal of Physical Chemistry C*, 111(46):17404–17408, November 2007.

[59] T. Hu, F. Zhang, Z. Xu, S. Zhao, X. Yue, and G. Yuan. *Synthetic Metals*, 159(7-8):754–756, April 2009.

[60] K. Sugiyama, H. Ishii, Y. Ouchi, and K. Seki. *Journal of Applied Physics*, 87(1):295–298, 2000.

[61] J. R Durrant, P. M Sommeling, and N. J Bakker. *Journal of Physical Chemistry C*, 111:14001–14010, 2007.

[62] V. Shklover, M.-K. Nazeeruddin, S. M. Zakeeruddin, C. Barbé, a. Kay, T. Haibach, W. Steurer, R. Hermann, H.-U. Nissen, and M. Grätzel. *Chemistry of Materials*, 9(2):430–439, February 1997.

[63] A. Hugot-Le Goff, S. Joiret, and P. Falaras. *The Journal of Physical Chemistry B*, 103(44):9569–9575, November 1999.

[64] W. Ma, Z. Lu, and M. Zhang. *Applied Physics A: Materials Science & Processing*, 66(6):621–627, June 1998.

[65] H. Greijer, J. Lindgren, and A. Hagfeldt. *The Journal of Physical Chemistry B*, 105(27):6314–6320, July 2001.

[66] K. S Finnie, J. R Bartlett, and J. L Woolfrey. *Langmuir*, 7463:2744–2749, 1998.

[67] L. C. T. Shoute and G. R. Loppnow. *Journal of the American Chemical Society*, 125(50):15636–46, December 2003.

[68] A. Marti, J. L. Balenzategui, and R. F. Reyna. *Journal of Applied Physics*, 82(8):4067, 1997.

[69] B.A. and Gregg and M.C. Hanna. No Title. *J. Appl. Phys.*, 93:3605, 2003.

[70] H. Tian, L. Liu, B. Liu, S. Yuan, X. Wang, Y. Wang, T. Yu, and Z. Zou. *Journal of Physics D: Applied Physics*, 42(4):045109, February 2009.

[71] S. Nakade, T. Kanzaki, Y. Wada, and S. Yanagida. *Langmuir : the ACS journal of surfaces and colloids*, 21(23):10803–7, November 2005.

[72] J. Bisquert and V. Vikhrenko. *The Journal of Physical Chemistry B*, 108(7):2313–2322, February 2004.

[73] N.W Duffy, L.M Peter, R.M.G Rajapakse, and K.G.U Wijayantha. *Electrochemistry Communications*, 2(9):658–662, September 2000.

[74] N W Duffy and L M Peter. *Electrochemistry Communications*, 2:262–266, 2000.

[75] L M Peter, N W Duffy, and R L Wang. *Journal of Electroanalytical Chemistry*, 525:127– 136, 2002.

[76] M. Nazeeruddin, M. K.; De Angelis, F.; Fantacci, S.; Selloni, A.; Viscardi, G.; Liska, P.; Ito, S.; Takeru, B.; Graetzel. *J. Am. Chem. Soc.*, 127:16835–16847, 2005.

[77] M. Nazeeruddin, M.K.; Klein, C.; Liska, P.; Graetzel. *Coord. Chem. Rev.*, 249:1460–1467, 2005.

[78] M. Wang, P.; Zakeeruddin, S. â.; Moser, J. â.; Humphry-Baker, R.; Comte, P.; Aranyos, V.; Hagfeldt, A.; Nazeeruddin, M. â.; Grätzel. *Adv. Mater.*, 16:1806–1811, 2004.

[79] W. Wu, J. Yang, J. Hua, J. Tang, L. Zhang, Y. Long, and H. Tian. *Journal of Materials Chemistry*, 20(9):1772, 2010.

[80] A. Abbotto, C. Barolo, L. Bellotto, F. De Angelis, M. Grätzel, N. Manfredi, C. Marinzi, S. Fantacci, J. Yum, and M. K Nazeeruddin. *Chemical communications (Cambridge, England)*, (42):5318–20, November 2008.

[81] P. Asghar, M.I.; Miettunen, K.; Halme, J.; Vahermaa, P.; Toivola, M.; Aitola, K.; Lund. *Energy Environ. Sci.*, 3:418–426, 2010.

[82] M. J. Am. Chem. Soc. Bessho, T.; Yoneda, E.; Yum, J.-H.; Guglielmi, M.; Tavernelli, I.; Imai, H.; Rothlisberger, U.; Nazeeruddin, M.K.; Graaetzel. 131:5930–5934, 2009.

[83] F. Flamigni, L.; Barbieri, A.; Sabatini, C.; Ventura, B.; Barigelletti. *Top. Curr. Chem.*, 281:143–203, 2007.

[84] D. Valore, A.; Cariati, E.; Dragonetti, C.; Righetto, S.; Roberto, D.; Ugo, R.; De Angelis, F.; Fantacci, S.; Sgamellotti, A.; Macchioni, A.; Zuccaccia. *Chem. Eur. J.*, 16:4814–4825, 2010.

[85] S. R. Baldo, M. A.; Lamansky, S.; Burrows, P. E.; Thompson, M. E.; Forrest. *Appl. Phys. Lett.*, pages 4–6.

[86] M. K. Baranoff, E.; Yum, J. -H.; Jung, I.; Vulcano, R.; Grätzel, M.; Nazeeruddin. *Chem. Asian J.*, 5:496–499, 2010.

[87] K. J. Koizumi, T.-A.; Tomon, T.; Tanaka. *Organomet. Chem.*, 690:4272–4279, 2005.

[88] G. Wadman, S.H.; Kroon, J.M.; Bakker, K.; Lutz, M.; Spek, A.L.; van Klink, G.P.M.; van Koten. *Chem. Commun.*, pages 1907–1909.

[89] C.P. Bomben, P.G.; Koivisto, B.D.; Berlinguette. *Inorg. Chem.*, 49:4960–4971, 2010.

[90] C. P. omben, P. G.; Robson, K. C. D.; Sedach, P. A.; Berlinguette. *Inorg. Chem.*, 48:9631–9643, 2009.

[91] A. Coluccini, C.; Manfredi, N.; Herrera Calderon, E.; Salamone, M.; Ruffo, R.; Roberto, D.; Lobello, M. G.; De Angelis, F.; Abbotto. *Eur. J. Org. Chem.*, pages 5587–5598, 2011.

[92] N. R. Neale, N. Kopidakis, J. van de Lagemaat, M. GrÃ€tzel, and Arthur J. Frank. *The Journal of Physical Chemistry B*, 109(49):23183–23189, 2005. PMID: 16375281.

[93] C. Zafer, K. Ocakoglu, C. Ozsoy, and S. Icli. *Electrochimica Acta*, 54(24):5709–5714, October 2009.

[94] I. J Le Bahers, T.; Labat, F.; Pauporté, T.; Lainé, P. P.; Ciofini. *J. Am. Chem. Soc.*, 133:8005–8013, 2011.

[95] J. T. Yan, S.-G.; Hupp. *J. Phys. Chem.*, 100:6867–6870, 1996.

[96] L. Beverina and P. Salice. *European Journal of Organic Chemistry*, 2010(7):1207–1225, March 2010.

[97] M. K.; Ko Paek, S.; Choi, H.; Kim, C.; Cho, N.; So, S.; Song, K.; Nazeeruddin. *J. Chem. Comm.*, 47:2874, 2011.

[98] M. K. Beverina, L.; Ruffo, R.; Mari, C. M.; Pagani, G. A.; Sassi, M.; De Angelis, F.; Fantacci, S.; Yum, J.-H.; Grätzel, M.; Nazeeruddin. *ChemSusChem*, 2:621, 2009.

[99] M. K. Shi, Y. Hill, R. B. M.; Yum, J. H.; Dualeh, A.; Barlow, S.; Graetzel, M.; Marder, S. R.; Nazeeruddin. *Angew. Chem. Int. Ed.*, 50:6619, 2011.

[100] C.-G. Li, J.-Y.; Chen, C.-Y.; Lee, C.-P.; Chen, S.-C.; Lin, T.-H.; Tsai, H.-H.; Ho, K.-C.; Wu. *Org. Lett.*, 12:5454, 2010.

[101] R. Li, R.; Liu, J.; Cai, N.; Zhang, M.; Wang. *J. Phys. Chem. B*, 114:4461, 2010.

[102] D. P. Hagberg, X. Jiang, E. Gabrielsson, M. Linder, T. Marinado, T. Brinck, A. Hagfeldt, and L. Sun. *J. Mater. Chem.*, 19:7232–7238, 2009.

[103] X. Jiang, T. Marinado, E. Gabrielsson, D. P. Hagberg, L. Sun, and A. Hagfeldt. *The Journal of Physical Chemistry C*, 114(6):2799–2805, February 2010.

[104] S. Das S. Alex , U. Santhosh. *J. Photochem. Photobiol. A*, 172:63 –71, 2005.

[105] S. Kuster, F. Sauvage, Md. K. Nazeeruddin, M. Grätzel, F. a. Nüesch, and T. Geiger. *Dyes and Pigments*, 87(1):30–38, September 2010.

[106] T. Geiger, S. Kuster, J. Yum, S. Moon, M. K. Nazeeruddin, M. Grätzel, and F. Nüesch. *Advanced Functional Materials*, 19(17):2720–2727, September 2009.

[107] M. Graetzel A. Burke , L. Schmidt-Mende , S. Ito. *Chem. Commun.*, pages 234 –236, 2007.

[108] M. K. Nazeeruddin J.-H. Yum, P.Walter, S. Huber, D. Rentsch, T. Geiger, F. Nuesch, F. De Angelis, M. Gratzel. *J. Am. Chem. Soc.*, 129:10320, 2007.

[109] Gratzel A. Burke, L. Schmidt-Mende, S. Ito, M. *Chem. Commun.*, pages 234–236, 2007.

[110] F. Nuesch T. Geiger, S. Kuster, J.-H. Yum, S.-J. Moon, M. K. Nazeeruddin, M. Gratzel. *Adv. Funct. Mater.*, 19:2720, 2009.

[111] I. Concina, E. Frison, A. Braga, S. Silvestrini, M. Maggini, G. Sberveglieri, A. Vomiero, and T. Carofiglio. *Chemical communications (Cambridge, England)*, 47(42):11656–8, November 2011.

[112] J. H. Im C. -R. Lee, H. -S. Kim, I. -H. Jang and N. G. Park. *ACS Appl. Mater. Interf.*, 3:1953, 2011.

[113] A. H. Tian, X. Yang, R. Chen, R. Zhang, Hagfeldt and L. Sun. *J. Phys. Chem. C*, 112:11023, 2008.

[114] B. Y. Liang, Peng and J. Chen. *J. Phys. Chem. C*, 114:10992, 2010.

[115] M. Law, L. E Greene, A. Radenovic, T. Kuykendall, J. Liphardt, and P. Yang. *Journal of Physical Chemistry B*, 110:22652–22663, 2006.

[116] Z. Wang, M. Yanagida, K. Sayama, and H. Sugihara. *Chemistry of Materials*, 18(12):2912–2916, June 2006.

[117] J. T. Ishihara, S. Sano and K. Toyoda. *J. Appl. Phys.*, 44:2780, 2005.

[118] A. Hagfeldt T. Marinado, M. Hahlin, X. Jiang, M. Quintana, E. M. J. Johansson, E. Gabrielsson, S. Plogmaker, D. P. Hagberg, G. Boschloo, S. M. Zakeeruddin, M. Grätzel, H. Siegbahn, L. Sun and H. Rensmo 11903. *J. Phys. Chem. C*, 114, 2010.

[119] T. Watson, P. Holliman, and D. Worsley. *Journal of Materials Chemistry*, 21(12):4321, 2011.

[120] A. B. Walker A. Peic, D. Staff, T. Risbridger, B. Menges, L. M. Peter and P. J. Cameron. *J. Phys. Chem. C*, 115:613, 2011.

[121] B. Peng C. P. Leon, L. Kador and M. Thelakkat. *J. Phys. Chem. B*, 110:8723, 2006.

[122] Chem. Commun. P. J. Holliman, M. L. Davies, A. Connell, B. V. Velasco and T. M. Watson. *Chem. Commun.*, 46:7256, 2010.

[123] M. R. Baklanov, K. P. Mogilnikov, V. G. Polovinkin, and F. N. Dultsev. *Journal of Vacuum Science & Technology B: Microelectronics and Nanometer Structures*, 18(3):1385, 2000.

[124] X. Li, J. Gao, L. Xue, and Y. Han. *Advanced Functional Materials*, 20(2):259–265, January 2010.

[125] M. K. Nazeeruddin F. De Angelis, S. Fantacci, E. Mosconi and M. Graetzel. *J. Phys. Chem. C*, 115:8825, 2011.

[126] Chang-Ryul Lee, Hui-Seon Kim, In-Hyuk Jang, Jeong-Hyeok Im, and Nam-Gyu Park. *ACS applied materials & interfaces*, 3(6):1953–7, June 2011.

[127] A. Hauch and A. Georg. *Electrochimica Acta*, 46:3457– 3466, 2001.

[128] W.J. Lee, E. Ramasamy, D.-Y. Lee, and J.-S. Song. *Solar Energy Materials and Solar Cells*, 92(7):814 – 818, 2008.

[129] B. Koo, D. Lee, H. Kim, W. Lee, J. Song, and H. Kim. *Journal of Electroceramics*, 17(1):79–82, September 2006.

[130] S. U. Lee, W. S. Choi, and B. Hong. *Solar Energy Materials and Solar Cells*, 94(4):680 – 685, 2010.

[131] X. Wang, L. Zhi, and K. Mu. *Nano Letters*, 8(1):323–327, 2008.

[132] W. Lee, E. Ramasamy, D. Lee, and J. Song. *ACS applied materials & interfaces*, 1(6):1145–9, June 2009.

[133] M. W Rowell, M. A Topinka, M. D Mcgehee, G. Dennler, N. S. Sariciftci, L. Hu, and G. Gruner. *Applied Physics Letters*, 88:159–161, 2006.

[134] E. Ramasamy, W. J. Lee, D. Lee, and J. Song. *Applied Physics Letters*, 90:23–25, 2007.

[135] T Du, S A Getty, Enrique Cobas, and M S Fuhrer. *Nano Letters*, 4(1):35–39, 2004.

[136] T Dikonimos Makris. *Diamond and Related Materials*, 13(2):305–310, February 2004.

[137] T Makris, R Giorgi, N Lisi, L Pilloni, and E Salernitano. *Diamond and Related Materials*, 14(3-7):318–322, March 2005.

[138] A Chuang, B Boskovic, and J Robertson. *Diamond and Related Materials*, 15(4-8):1103–1106, April 2006.

[139] S. Kurita, a. Yoshimura, H. Kawamoto, T. Uchida, K. Kojima, M. Tachibana, P. Molina-Morales, and H. Nakai. *Journal of Applied Physics*, 97(10):104320, 2005.

[140] S. Ahmad, J.H. Yum, Z. Xianxi, M. Grätzel, H. Butt, and M. K. Nazeeruddin. *Journal of Materials Chemistry*, 20(9):1654, 2010.

[141] S. Ahmad, M Deepa, and S Singh. *Langmuir : the ACS journal of surfaces and colloids*, 23(23):11430–3, November 2007.

[142] H. Tian, Z. Yu, A. Hagfeldt, L. Kloo, and L. Sun. *Journal of the American Chemical Society*, 133(24):9413–22, June 2011.

[143] J.H. Yum, R. Humphry-Baker, S. M. Zakeeruddin, M. K. Nazeeruddin, and M. Grätzel. *Nano Today*, 5(2):91–98, April 2010.

[144] H. Tsao, C. Yi, T. Moehl, J.H. Yum, S. M Zakeeruddin, M. K Nazeeruddin, and M. Grätzel. *Chemical Communications*, 4(5):591–4, May 2011.

[145] J. Bisquert. *Physical Review B*, 77(23):1–15, June 2008.

[146] Q. Wang, J. Moser, and M. Grätzel. *The journal of physical chemistry. B*, 109(31):14945–53, August 2005.

[147] R Kern. *Electrochimica Acta*, 47(26):4213–4225, October 2002.

[148] V. Yong, Se. Ho, and R. P. H. Chang. *Applied Physics Letters*, 92(14):143506, 2008.

[149] R. Lee, Y. Huang, J. Chang, J. Hwang, Y. Chen, and R. Jeng. *Polymers for Advanced Technologies*, 22(12):1650–1657, December 2011.

[150] J. Bisquert, F. Fabregat-Santiago, I. Mora-Seró, G. Garcia-Belmonte, E. M. Barea, and E. Palomares. *Inorganica Chimica Acta*, 361(3):684–698, February 2008.

[151] J. van de Lagemaat, N.-G. Park, and a. J. Frank. *The Journal of Physical Chemistry B*, 104(9):2044–2052, March 2000.

[152] J. Bisquert. *The Journal of Physical Chemistry B*, 106(2):325–333, January 2002.

[153] F. Fabregat-Santiago, J. Bisquert, E. Palomares, S. a. Haque, and J. R. Durrant. *Journal of Applied Physics*, 100(3):034510, 2006.

[154] M. Wang, P. Chen, R. Humphry-Baker, S. M Zakeeruddin, and M. Grätzel. *Chemphyschem : a European journal of chemical physics and physical chemistry*, 10(1):290–9, January 2009.

[155] a. Zaban, J. Zhang, Y. Diamant, O. Melemed, and J. Bisquert. *The Journal of Physical Chemistry B*, 107(25):6022–6025, June 2003.

[156] H. Wang, P. G Nicholson, L. Peter, S. M Zakeeruddin, and M. Graetzel. *Journal of Physical Chemistry C*, pages 14300–14306, 2010.

[157] T. Hoshikawa, M. Yamada, R. Kikuchi, and K. Eguchi. *Journal of Electroanalytical Chemistry*, 577(2):339–348, April 2005.

[158] J. Bisquert, G. Garcia-Belmonte, F. Fabregat-Santiago, N. S. Ferriols, P. Bogdanoff, and E. Pereira. *The Journal of Physical Chemistry B*, 104(10):2287–2298, March 2000.

[159] A. Zaban, A. Meier, and B. A. Gregg. *The Journal of Physical Chemistry B*, 101(40):7985–7990, October 1997.

[160] F Lamantia, J Vetter, and P Novak. *Electrochimica Acta*, 53(12):4109–4121, May 2008.

List of Figures

List of papaers

Dell'Orto E., Raimondo L., Sassella A., Abbotto A., Dye-sensitized solar cells: spectroscopic evaluation of dye-loading on TiO2, Journal of Materials Chemistry. In submission article.

Dell'Orto E, Ruffo R., La Mantia F., Abbotto A., Calderon Herrera E., Mari C., *Study of counter-electrode influence in DSSC performances by EIS using a three-electrodes system, Electrochemical Communication*. In submission article.

Abbotto A., Dell'Orto E., Coluccini C., Manfredi N., Trifiletti V., Caccamo L., Acciarri M., Colombo A., Dragonetti C., Ordanini S., Roberto D., Valore A., *Thiocyanate-free cyclometalated ruthenium sensitizers for solar cells based on heteroaromatic-substituted 2-arylpyridines*, The Journal of Physical Chemistry C.

Delcamp J. H., Yum J.H., Dell'Orto E., Shi Y., Marder S.Y., Nazeeruddin M. K. and Grätzel M., *A Near Ideal Panchromatic Response in DSCs with a Squaraine Sensitizer, Angewandte Chemie International Edition*. Submitted.

Ahmad S., Yum J. H., Dell'Orto E., Nazeeruddin M. K. and Grätzel M., *et al.; PEDOT free dye-sensitized solar cells based on poly(3,4-ethylenedioxythiophene) counter electrode*, in preparation.

Park J., Barolo C.,Barberoa N., Magistris C., Quagliotto P., Viscardia G., Dell'Orto E., Yoon J., Yum J-H,Gratzel M., *A high-Efficiency and Stable Symmetrical Panchromatic Squaraine for Dye-Sensitized Solar Cells*, in preparation.

Acknowledgments

CORIMAV for Ph. D. position.

Fondazione Cariplo (Grant No. 2008-2205 and No. 2010-0525) and MIUR-PRIN (Grant No. 2008CSNZFR) for financial support.

ENEA MAT-TEC department and LPI-EPFL for materials and instruments.

HOPP-lab group: Professor Alessandro Abbotto, Dr. Lorenzo Caccamo, Dr. Carmine Coluccini, Dr. Norberto Manfredi, Dr. Valentina Leandri, Dr. Vanira Trifiletti.

A thanks to Dr. Riccardo Ruffo and Dr. Erika C. Herrera.

MAT-TEC group: Dr. Rossella Giorgi, Dr. Serena Gagliardi, Dr. Loenardo Giorgi, Dr. Nicola Lisi, Dr. Elena Salernitano, Dr. Teo Makris.

LPI-EPFL group, expecially Dr. J.H. Yum, Dr. Nazeeruddin and Professor Graetzel.